University of Amsterdam

Master of Science in Physics
Theoretical Physics

Master Thesis

Indirect Dark Matter Searches with Cosmic X-ray Background Analysis

Forecasting for keV Sterile Neutrino Dark Matter detection from anisotropies in the X-ray sky

---

by

Andrea Chiappo
10408460

60 ECTS
September 2013 - June 2014

Supervisor:
Dr Shin'ichiro Ando

Daily Supervisors:
Dr Fabio Zandanel
Dr Irene Tamborra

Examiner:
Dr Gianfranco Bertone

GRAPPA Institute

To my parents

Ai miei genitori

A gno pari e me mari

Contents

Abstract

Sterile neutrinos represent viable dark matter candidates and their existence may be indirectly inferred by detecting their decays products. Theoretical calculations predict the existence of a sub-dominant, one-loop channel where the sterile neutrino radiatively decays into an active neutrino and a photon, with a decay time of the order of 10^{22} s, therefore exceeding the age of the Universe (10^{18} s). Being the mass range of the sterile neutrino 2-10 keV, favoured by the latest X-ray observations of dwarf spheroidal galaxies and clusters of galaxies, the resulting photon should be detectable in the soft X-ray band (1-5 keV). The sterile neutrino decay should yield a cosmic background correlated with the large-scale structure of the Universe, i.e. with dark matter halos, in particular with large groups and clusters of galaxies. The angular power spectrum of the anisotropic component (APSAC) of X-ray all-sky maps should enclose the indication for the existence of this particle. The possible detection of the decay photon would, therefore, represent a smoking-gun evidence for the sterile neutrino existence. In this work we construct the predictions for the APSAC of the X-ray cosmological background, which we assume to be dominated by the heavy sterile neutrino decay signal. This is done adopting the sensitivity of two future X-ray space telescopes: eROSITA, which will perform an all-sky survey in the Soft X-ray energy band, and Astro-H, which will perform deep-field surveys of astrophysical systems. To further refine the predictions and in order to assure detectability of the X-ray background anisotropies, the mean extragalactic intensity of the considered decay process is compared with the Galactic foreground emission, due to heavy sterile neutrinos decaying within our galaxy. It is found that eROSITA will be able to observe more features of the predicted APSAC, on a broader range of multipoles. We also show that the Galactic signal prevails up to high latitudes and the extragalactic mean component only dominates on directions nearly opposite to the Galactic Centre.

Chapter 1

Introduction

The current cosmological model indicates that we live in a nearly flat universe, meaning that the curvature parameter of spacetime k is close to zero. The complex large scale structure that we observe resulted from the evolution of an initial perfectly homogeneous distribution of matter due to the growth of primordial density perturbations [1]. These perturbations are present at all cosmological scales and should have originated from quantum fluctuations stretched during a period of inflation at very early times. The ΛCDM model also gives a precise indication on the fundamental constituents of the Universe, requiring the presence of three main ingredients arranged in the following percentages: approximately 4% of the entire energy content constitutes of ordinary (i.e. baryonic) matter, 26% of dark matter (DM) and the remaining 70% is in the form of dark energy. The first proposal for the existence of DM dates back to 1933 and is attributed to Fritz Zwicky [2], who, by observing the Coma cluster, noticed the existence of unseen matter necessary to explain the radial velocities of the cluster's member galaxies. The second most famous indication came during the 70's, when astronomers measured the velocities of spiral galaxies and obtained flat profiles [3] - different from the expected Keplerian - which could be naturally explained by postulating the presence of an invisible massive component in the outskirts of such systems. In recent years, the largely increased technological possibilities for scientific surveys have allowed to reveal several other phenomenological hints of DM [4]; among the most important results we mention studies of gravitational lensing [5], of structure formation [6] and of big bang nucleosynthesis [7]. One of the strongest and most recent experiments supporting the DM hypothesis, and more generally the cosmic inventory outlined above, comes from the analysis of the cosmic microwave background (CMB) [8]. Although modified gravity models [9] have also been proposed to justify the above anomalies, the most consistent way to simultaneously explain all such phenomena is to postulate the existence of a new particle consisting of DM.

As the phenomenological evidence uncontroversially requires a DM component in the Universe, the greatest source of mystery that is left to be unveiled regards its nature. Various candidates have been proposed during the last decades; for a review on the claimed possibilities refer to Ref. [10]. In particular, being not hadronic, the corresponding particle cannot interact via the colour force and, as it does not absorb or emit light in any energy band, it does not interact electromagnetically either. These features together strongly narrow the possibilities, eventually requesting the introduction of new, beyond

the standard model (BSM) particles, consequentially leading to the necessity of new physics. In the most common scenario, DM is the Weakly Interactive Massive Particle (WIMP) [11], a class of particles with a typical mass ranging from 10 GeV to 10 TeV and, as the name suggests, by an extremely small interaction probability with itself and with baryonic matter. A group of WIMPs that has received great attention arises from an extension of the Standard Model (SM) of Particle Physics called Super Symmetry (SUSY); among the various candidates, some of the most famous are: the *neutralino*, the *gravitino* and the *axino* [12]. Because of the great theoretical plausibility of SUSY and the high suitability of DM in the form of WIMPs, there are ongoing intensive searches for them with different approaches. Direct detection experiments aim at observing nuclear recoils of liquid Xenon resulting from collisions with WIMPs [13]; the possibility of creating a WIMP and successively detecting missing energy in decay processes at accelerator facilities, above all the Large Hadron Collider [14]; finally, the decay or annihilation signals of WIMPs pervading the Universe are investigated in the gamma-ray sky [15]. Despite the premises, all these techniques have been unsuccessful so far, thus motivating the necessity to consider other possible scenarios and new candidate particles.

An accredited and interesting alternative emerges from the anomalies in the neutrino sector of the SM. In its original formulation, the SM (active) neutrinos were assumed to be massless neutral leptons. The discovery of a non-zero mass difference between neutrino flavours at oscillations experiments, such as LSND [16], has been interpreted as the evidence for the existence of a light (eV) fourth neutrino species, the **sterile neutrino**. This finding supported the hypothesis of a heavy right-handed neutral lepton which could have great phenomenological implications, above all the possibility that it represents the long sought for DM. In this case, its cosmological signature - a radiative decay mode - could lead to the opportunity of indirectly inferring its existence in the Universe. The importance of identifying DM and characterising its nature requires all feasible scenarios to be investigated, in particular those theoretically interesting and experimentally accessible. Being the sterile neutrino among them, highlights the priority of pursuing its studies and searches.

The aim of this project is to prove that the next generation of X-ray space-borne observatories, e.g. eROSITA and Astro-H, will have sufficient sensitivity to indirectly infer DM, in the form of a keV sterile neutrino, by detecting the trace of its decay. Differently from previous approaches, which relied on the detection of the decay line in the flux of astrophysical objects, this will be primarily achieved by constructing the angular power spectrum of the anisotropic component (APSAC) of the X-ray emission resulting from the sterile neutrino decay. Successively, the mean extragalactic component will be compared to the Galactic foreground emission, due to sterile neutrinos decaying within our galaxy, in order to determine the range of Galactic latitudes at which the extragalactic signal will be predominant. In addition to this, the APSAC will be cross-correlated between different energies, in order to give an instrument to detect the contamination from the astrophysical background. Finally, we will investigate the implications on the above predictions in relation to the nature of the sterile neutrino DM, i.e. whether it would constitute *warm dark matter* (WDM) or *cold dark matter* (CDM).

This thesis is organised in the following way: Chapter II will briefly present the theoretical motivations for postulating the existence of (at least one) sterile neutrino, together with its most relevant features for this projects, and the framework within which it has

been accommodated, the νMSM; in Chapter III the indirect detection strategies and the auxiliary techniques that have been adopted are introduced. From this point onward we report the original results of this work: the detailed derivation and the construction of the predictions for the shape of the APSAC can be found in Chapter IV; the comparison of the Galactic foreground emission with the mean extragalactic intensity is given in Chapter V; Chapter VI deals with the cross correlation of the decay signal at different energies. Finally, the conclusions are summarised in Chapter VII.

Chapter 2

Sterile Neutrinos

The SMs of Particle Physics and Cosmology have allowed great insight into the world of elementary particles and fundamental interactions, on one side, and a deep understanding of the structure and composition of the Universe, on the other. Nevertheless, in the last decades, it has become clear that, despite their successfulness and mathematical beauty, they are not a final and complete theory of nature. Indeed, the SMs still fail to explain a number of observed phenomena in particle physics, astrophysics and cosmology. These BSM phenomena are: neutrino masses and oscillations (transitions between neutrinos of different flavours), baryon asymmetry (excess of matter over antimatter in the Universe), inflation (a period of accelerated expansion in the early Universe), dark energy (late-time accelerated expansion of the Universe), dark radiation (unexplained excess of relativistic degrees of freedom) and DM.
The problem of neutrino non-zero masses, and the necessity to include and characterise the nature of DM, could be jointly solved by introducing a fourth neutrino. Indeed, theoretical arguments [17] and experimental results [18] favour the existence of a new species, a sterile neutrino ν_s, which would also have great observable implications for astrophysics and cosmology as it could explain, among others, pulsar velocities [19] and also represent a viable DM candidate [20]. As it will be explained in greater detail below, the various BSM extensions, which have been developed to accommodate such particle, do not give constraining indications for its mass. Hence a wide spectrum of different scenarios is possible, ranging from few eV (light ν_s) up to hundreds of MeV (heavy ν_s).
In this chapter we will summarise the state-of-the-art knowledge regarding this particle, focusing on its importance for the purpose of this project.

2.1 Theoretical motivations for the existence of ν_{S}

Active neutrinos were originally devised as massless neutral fermions transforming as components of the electroweak (EW) SU(2) doublets of the SM of Particle Physics [22]. They appear in three different flavours, one per each known lepton generation (electron, muon, tau), and carry the corresponding lepton number $\mathrm{L}_{e,\mu,\tau}$. Despite its successfulness in explainig and predicting many phenomena [21], this framework became faulty in the late 60's due to the emergence of the so-called "solar neutrino problem"[23], where the measured electron neutrino flux from the Sun disagreed with the predictions. This shortcoming in the neutrino sector of the SM led to the first proposal of neutrino oscillations

between flavours, which were later experimentally confirmed by MINOS [25] and KamLAND [24]. Such discovery hinted the non-zero mass of active neutrinos, in clear contrast with SM assumptions. This feature suggested the existence of a fourth massive neutrino species which, in order to comply the prescriptions of the SM neutrino sector, needs to be a gauge-singlet. This peculiarity implies that such particle is right-handed under the EW gauge group SU(2) and, since the EW bosons $W^{\pm}$ only couple to left-handed components, it does not participate to SM interactions, hence it is *sterile*.

The most natural way to introduce active neutrino masses including sterile neutrinos is achieved by adding to the SM Lagrangian, $\mathcal{L}_{SM}$, several electroweak singlets $N_{\rm s}$ (s $= 1, \ldots, n$) to build the seesaw Lagrangian [26]

$$\mathcal{L} = \mathcal{L}_{SM} + i\, \bar{N}_{\rm s}\, \not{\partial}\, N_{\rm s} - y_{\rm as}\, H^{\dagger}\, \bar{L}_{\rm a}\, N_{\rm s} - \frac{m_{\rm s}}{2}\, \bar{N}^{c}_{\rm s}\, N_{\rm s} + h.c.$$

where $H^{\dagger}$ is the complex conjugate of the Higgs field, $y_{\rm as}$ the Yukawa coupling, $\bar{L}_{\rm a}$ are the electroweak doublets corresponding to active neutrinos and $\bar{N}^{c}_{\rm s}$ are the charge-conjugated gauge-singlets.
The neutrino mass eigenstates $\nu^{(m)}_{\rm i}$ (i $= 1, \ldots, n+3$) correspond then to linear combinations of the weak eigenstates $\{\nu_{\rm a}, N_{\rm s}\}$, i.e. active (a) and sterile (s), and are obtained by the diagonalising the $(n+3) \times (n+3)$ Seesaw mass matrix [26]

$$\mathcal{M}^{(n+3)} = \begin{pmatrix} 0 & y_{\rm as}\, \langle H \rangle \\ \\ y_{\rm as}\, \langle H \rangle & \mathrm{diag}\{m_1, \ldots, m_n\} \end{pmatrix}. \tag{2.1.1}$$

The mass eigenvalues will split into two distinct groups: lighter states with masses of the order of [26]

$$m(\nu^{(m)}_{1,2,3}) \sim \frac{y^2_{\rm as}\, \langle H \rangle^2}{m_{\rm s}}\,,$$

corresponding to (three known) active neutrinos, and heavier eigenstates with masses of the order of $m_{\rm s}$

$$m(\nu^{(m)}_{\rm s}) \sim m_{\rm s} \;\; (s > 3)\,,$$

relative to the postulated sterile neutrinos [26].
With this mechanism the new right-handed gauge-singlet fermions can be made heavy even for very light active neutrinos. The ratio between the masses of the two will be governed by the magnitude of the mixing angle between their weak eigenstates, which is of the order of

$$\theta^2_{\rm as} \sim \frac{y^2_{\rm as}\, \langle H \rangle^2}{m^2_{\rm s}}\,.$$

As a consequence of this, the smallness of active neutrino masses can be due to either large $\theta^2_{\rm as}$ and large $m_{\rm s}$ or small $\theta^2_{\rm as}$ and small $m_{\rm s}$. More generally, this will lead to a two-variables parameter space which will encompass all possible combinations of $(m_{\rm s}, \theta^2_{\rm as})$ consistent with the inferred active neutrino masses. The upshot is that the mass spectrum of $\nu_{\rm s}$ is very broad and can range from few eV all the way up to the EW scale ($M_{\rm EW} \simeq 246$ GeV).
Since a sterile neutrino with mass $m_{\rm s} >> M_{\rm EW}$ would be practically unobservable, we will discuss three possible mass scales below the EW, namely eV, keV and MeV:

- eV
  This is the mass region where most neutrino experiments have found hints favouring the existence of a fourth neutrino species [24, 25, 27]. Along with supporting results, however, there are also measurements which contrast such scenario; examples are LEP and KARMEN [28]. In recent years, a huge experimental effort has been devolved to testing the existence of a fourth neutrino [31] and more accurate indications are expected to emerge from the ongoing CeLAND [32] and KamLAND [24]. These light sterile neutrinos have been considered as possible DM candidates, although they would represent hot DM, thus conflicting with cosmological observations [29, 30].

- keV
  A ν_{s} with this mass has received great attention by the scientific community as it could simultaneously explain active neutrino masses (via the Seesaw mechanism described above), the so-called pulsar kicks [19] and also represent a DM candidate largely consistent with cosmological constraints [33].

- MeV
  The investigation of a heavy sterile neutrino is physically interesting because its decay into leptons and photons in the Early Universe (cf. Section 2.2.2) would lead to a non-negligible contribution to the number of effective relativistic degrees of freedom (N_{eff}) [34]. Consequently, this could account for the BSM phenomena of dark radiation [35] and also help explaining the CMB-inferred value $N_{\mathrm{eff}} \gtrsim 3$ [8].

We will now analyse the demands that sterile neutrinos must satisfy in order to be considered a viable DM candidate, focusing also on whether they are WDM or CDM. We quickly remind that the former case refers to DM particles which decouple from radiation in the Early Universe while becoming non-relativistic, whereas the latter are DM particles which are already non-relativistic at decoupling.

2.2 Heavy ν_{s} as dark matter candidates

The absence of EW interactions with SM particles, except the small oscillations-induced mixing with active neutrinos, renders sterile neutrinos very attractive as DM candidate particles if they fulfill the following three requirements:

- **production mechanism (PM)**
  sterile neutrinos need to be produced in the correct amount and with properties that match cosmological [33] and astrophysical constraints [36].

- **sufficient stability**
  DM candidate particles must be stable and have a lifetime at least as long as the age of the Universe, so that their current abundance matches the inferred value of Ω_{DM}.

- **specific mass scale**
  similarly to the first point, the mass scale of the sterile neutrino DM must also comply with cosmological [33] and astrophysical constraints [36].

Each of the above points will be now briefly discussed, reporting the most recent experimental results.

2.2.1 Production mechanism

Sterile neutrinos can be produced in one or more of the following ways:

1. **Mixing with SM neutrinos**
   This itself separates into two distinct mechanisms:

   - Non-resonant oscillations: The so-called *Dodelson & Widrow* (DW) PM [20], was the first mechanism to be proposed. Sterile neutrinos are produced via oscillations with active neutrinos in the Early Universe, in presence of a negligible lepton asymmetry. The resulting particles are WDM candidates.
   - Resonant oscillations: The so-called *Shi & Fuller* (SF) PM [37], this is a modification of the previous in the presence of a non-zero lepton asymmetry in the Universe. Oscillations are enhanced by the Mikheev-Smirnov-Wolfenstein effect [38], leading to a greater abundance of relic sterile neutrinos with a lower average momentum. Hence $\nu_{\rm s}$ produced via the SF PM are CDM candidates.

2. **Higgs decay**
   A bulk of sterile neutrinos could be produced from decays of gauge-singlet Higgs bosons at the EW scale [39]. Consequently, the momenta of the sterile neutrinos are redshifted as the Universe cools down, rendering them CDM candidates.

3. **Non-thermal production**
   ν_s can be produced from their coupling to the inflaton [40] or the radion [41]. In this case, ν_s can be either Cold or Warm depending on the mass of the boson, e.g. if the inflaton's mass is lower than 1 GeV, they are WDM candidates, whereas if the sterile neutrinos are produced at higher energies, they are redshifted and become CDM candidates.

In all these production scenarios, sterile neutrinos are never in thermal equilibrium with the primordial plasma, hence their relic abundance would not correspond to the thermal relic abundance.
It is important to highlight that each proposed PM yields the $\nu_{\rm s}$ to be either Warm or Cold DM and this aspect has far-reaching implications for astrophysics, as it will be explained in the forthcoming sections.

2.2.2 Detection strategies

Despite the fact that, being a SM gauge-singlet, the ν_s is not expected to have SM weak interactions with baryonic matter, it is still possible to infer its existence, both directly and indirectly:

- **Direct detection**
  Current neutrino oscillation experiments, such as CeLand [32] and KamLand [24], should be able to detect oscillations of an active neutrino into a light sterile neutrino.

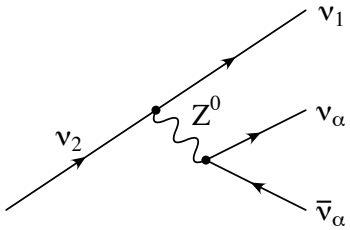

Figure 2.1: The principal decay mode for a massive singlet neutrinos. There are three light active neutrinos in the final state. (here $\alpha = e, \mu, \tau$) [44]

- **Indirect detection**
  Besides the gravitational effects of DM on radiation [5] and on baryonic matter [5, 6], there are several predicted decay channels for ν_s which yield detectable products: the dominant one, where ν_s decays into three active neutrinos (ν_a) via the exchange of a Z boson, has a Feynman diagram shown in Fig. 2.1 and is representable as follows

  $$\nu_\mathrm{s} \rightarrow 3\,\nu_\mathrm{a}\ .$$

  Along with this, there are several subdominant channels where ν_s decays into an ν_a plus either a photon or charged leptons; some examples are

  $$\nu_\mathrm{s} \rightarrow \nu_\mathrm{a} + \gamma \tag{2.2.1}$$

  $$\nu_\mathrm{s} \rightarrow \nu_\mathrm{a} + e^+ + e^-$$

  $$\nu_\mathrm{s} \rightarrow \nu_\mathrm{a} + \mu^+ + \mu^-$$

  $$\dots$$

The channel outlined in Eq. 2.2.1 represents the key feature of ν_s for the scope of this project: A two-body decay where one of the two products is a photon. Hence its normalised decay spectrum is given by

$$\frac{dN_\gamma}{dE_\gamma} = \delta_\mathrm{Dirac}\left(E_\gamma - \frac{m_\mathrm{s}}{2}\right)\ . \tag{2.2.2}$$

where E_γ is the photon energy and m_s the sterile neutrino mass.
The Feynman diagrams of two possible realisations of this process are shown in Fig. 2.2. Additionally, the decay rate of this process has been calculated to scale as the fifth power of the particle's mass and the square of the mixing angle with active neutrinos [43]

$$\Gamma_{\nu_\mathrm{s}\rightarrow\nu_\mathrm{a}+\gamma} \simeq 5.5 \times 10^{-22}\, sin^2(2\,\theta_\mathrm{as}) \left[\frac{m_\mathrm{s}}{\mathrm{keV}}\right]^5 s^{-1}\ . \tag{2.2.3}$$

For the mass range considered, this formula leads to a decay width several orders of magnitude smaller than the present-day value of the Hubble rate [8], $\Gamma_\mathrm{s} \ll H_0$, thus satisfying the stability requirement. The upshot is that sporadic ν_s decays should produce a narrow line in the spectra of DM-dominated astrophysical objects, with the following features: It should be peaked at $E_\gamma = m_\mathrm{s}/2$, but receiving contributions at lower energies from ν_s decaying at higher redshifts, and with broadening due to the characteristic velocity dispersion of DM, σ_v [42], in such objects.

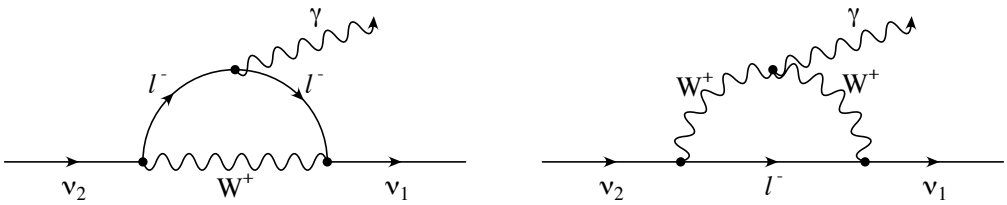

Figure 2.2: The principal radiative decay modes for a massive singlet neutrinos [44].

2.2.3 Mass constraints

If ν_s corresponds to the long sought for DM or at least a fraction thereof, then its mass must match several combined astrophysical restrictions. In detail, these are:

1. **Phace-space density bounds**
   This constraint arises from the application of the Tremaine-Gunn condition of compact objects [45]. This reads as follows: The phase-space density of DM, $\bar{f}$, in a given object cannot be greater than that of a degenerate Fermi gas

$$\bar{f} \leq \frac{m^4\, g}{(2\pi\hbar)^3} \tag{2.2.4}$$

   where m is the mass of DM and g its number of internal degrees of freedom.
   Limits can be obtained from this method by either direct observations of DM-dominated objects, such as the dwarf Spheroidal satellite galaxies (dShps) of the Milky Way (MW), or by utilising N-body simulations of such systems [46]. The upshot is a lower bound to the ν_s mass, set to $m_s > 2.5$ keV in the case of DM being generated via DW PM and to $m_s > 2$ keV for the SF PM case [46].
   Clearly this bound can be applied to any kind of fermionic DM.

2. **Lyman-α**
   The well-established connection between Lyman-α absorption lines in spectra of distant quasars, produced by clouds of neutral hydrogen distributed along the line-of-sight, and matter-density fluctuations at the submegaparsec scale, can be used to set another lower bound to the DM mass. This is because ν_s DM would lead to a cutoff on the power spectrum of such cosmological fluctuations, which can be directly linked to the particle's mass by evaluating its free-streaming lenght.
   The current limits impose that $m_s > 3.3$ keV [47].

3. **Galaxy substructure**
   There is a set of observational features of the MW which can be exploited to derive constraints on the DM particle's mass. E.g.

   - The number of observed dSphs of the MW is closely related to the mass and momentum distribution of DM: the lighter and faster the corresponding particles are, the higher the cutoff scale on the density perturbations which originate such substructures. Hence the size and number of dSphs can give an indication on the mass and nature of DM, in terms of whether it is WDM or CDM.
   - The measurement of the density profiles of dSphs can reveal the distribution of DM within such objects. This can also be utilised to discriminate between

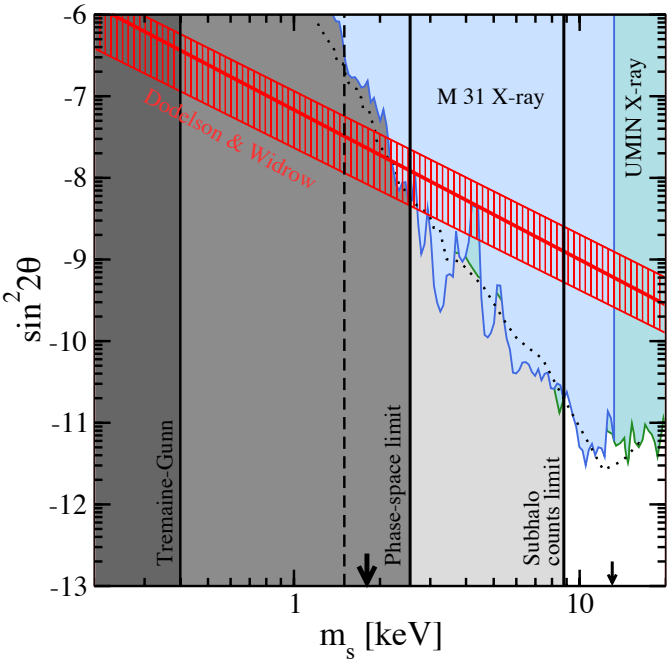

Figure 2.3: Constraints on the sterile neutrino parameters: blue shaded areas are excluded regions at 95% C.L. derived from Chandra M 31 X-ray observations. The vertical lines shown lower mass limits from Tremaine-Gunn phase-space condition. The lower limit obtained from Subhalo counts and the DW PM allowed parameters range is also shown. Figure taken from [46]

CDM and WDM as the former should lead to a cored profile, i.e. higher central densities due to the colder momentum distribution, whereas the latter to a shallower profile.

4. **X-ray observations**

Measurements of presumed DM-dominated objects - above all dSphs and clusters of galaxies - performed by X-ray space telescopes such as XMM-Newton [48], Suzaku [49] and Chandra [50], have allowed to set upper bounds on the DM mass. The ν_s decay within such astrophysical systems should, indeed, yield the following flux [51]

$$F = \frac{\Gamma_{\nu_s}}{4\pi m_s}\,\Omega_{\rm FOV}\,S_{\rm DM} \tag{2.2.5}$$

where $S_{\rm DM}$ is the DM mass column density averaged over the field-of-view, $\Omega_{\rm FOV}$, of the instrument.

Recalling Eq. 2.2.3, we see that the non-detection of the decay line translates into exclusions regions in the (m_s, θ_{as}) parameter space. An example is visible in Fig. 2.3, which reports a recent analysis of Chandra observations of M 31 (Andromeda Galaxy) [46]. Combining the phase-space lower bounds discussed above with the X-ray data, widely narrows the possible parameter space if the DW PM was to explain the totality of DM in the Universe. Moreover, this possibility is precluded if MW subhalo counts are included. The parameter space that is still allowed comprises ν_s with $m_s \gtrsim 8$ keV and $\theta_{as}^2 \lesssim 10^{-11}$ (the white area in the bottom right-hand corner of Fig. 2.3). These constraints are significantly relaxed in the SF PM scenario [46].

5. **Soft Gamma-ray observations**
   The possibility of a heavy, i.e. MeV scale, ν_s DM has been excluded by observations of the Diffuse Gamma-ray Background [52] in search for its decay line. Such bounds agree with calculations regarding SN1987A [52] and set an upper bound equal to $m_s < 40$ keV, with $\theta^2_{as} < 10^{-10}$.

We report two recent claims of detection of the ν_s decay line in the data from Chandra and XMM-Newton, both of which are largely consistent with the constraints presented above. The first indication emerges from the observations of Willman1, a MW dSphs, first by Chandra [53] and subsequently by XMM-Newton [54]. In both analyses of such dSphs, the authors detected a line in the X-ray flux at 2.5 keV, not corresponding to any atomic transition line of known elements. This led them to assert that it might correspond to the decay signal of a 5 keV sterile neutrino. The second claim is more recent and results from the analysis of the stacked XMM spectrum of 73 galaxy clusters [55]; the detected line has energy of approximatively 3.55 keV, suggesting possible existence of a sterile neutrino with mass of 7.1 keV. These two claimed values for m_s will be utilised at a later stage, when the predictions for the anisotropy of the ν_s decay will be presented.

2.3 *neutrino Minimal Standard Model*

We will conclude this chapter by briefly introducing a very interesting BSM extension that was developed during the 90s and which has received great attention because of its simplicity and because of the many SM issues it can simultaneously address.
Recalling the Seesaw mechanism presented in Section 2.1, we acknowledge that a broad range of values in Eq. 2.1.1 for the number n of additional sterile neutrinos is possible. In fact, unlike other fermions, the SM singlets are not subject to any constraint based on the anomaly cancellation [56] as these fermions do not couple to gauge fields. It can be shown that adding $n = 2$ sterile neutrinos is sufficient to explain active neutrino masses inferred from atmospheric and solar neutrino experiments [57]. However, if other astrophysical processes are considered, then this number must be higher; this is the case of nucleosynthesis [58], pulsar kicks [59] and supernova explosions [60], as well as DM [61].
Laine and Shaposhnikov [62] first noticed that a model with only $n = 3$ sterile neutrinos (N_1, N_2, N_3), one per generation of leptons, was the most economical theory that had enough degrees of freedom to simultaneously explain active neutrino masses and also provide a DM candidate. For this reason it was dubbed the *neutrino Minimal Standard Model* (νMSM).
Within this framework, the lightest of the newly introduced neutrinos, N_1, represents a viable DM candidate with mass ranging from few eV up to the keV scale, whereas the two heavier ones, N_2 and N_3, are assumed to be closely degenerate at about $1 - 10$ GeV scale. The latter two sterile neutrinos would have profound implications for the SM. Indeed, it was later noticed that they could provide a mechanism for baryogenesis, thus producing the inferred baryon asymmetry in the Universe [63], and also generate a non-negligible lepton asymmetry, which would be responsible for the sterile neutrino DM

production through the SF mechanism. Furthermore, detailed calculations [46] show how such a DM particle would be consistent with several constraints presented above. On one hand, it would predict a smaller amount of dSphs - in agreement with observations but in contrast with simulations [64] - thus having important implications for astrophysics, as it would strongly imply that these systems exist but cannot confine gas and remain completely dark. On the other hand, it could represent a feasible solution to the "too big to fail"problem [65], which can be expressed as follows: The discrepancy between the number of predicted substructures of a given mass, which would indeed be too big to be masked by galaxy formation processes, and the number of effectively observed ones. Resonantly produced sterile neutrino DM is expected to be "warm enough"to amend these issues but also "cold enough"to be in agreement with Lyman-α bounds. For an updated review on the most recent results on the νMSM refer to Ref. [66].

Chapter 3

Indirect detection techniques

The postulated existence of a radiative decay channel for ν_s renders its indirect detection by means of astronomical observations feasible. This feature, together with the evidence that DM is arranged in structures known as Dark Matter Halos (DMHs) [67], implies the most crucial aspect for this project: The decay of DM in the form of a ν_s should yield a cosmic background. Since the mechanism responsible for such background is a 2-body decay of a particle with mass of few keV, the resulting photon should have energy equal to $m_s/2$ and should, therefore, generate a Cosmic X-ray Background (CXB). The signature of the ν_s decay should be enclosed within the CXB in the form of an anisotropy in the angular power spectrum of the photon radiation, the APSAC, which would emerge from the analysis of all-sky maps in the corresponding energy band.
In this chapter we will present the three techniques that have been employed to study and predict the shape of the CXB.

3.1 Angular Power Spectrum C_l

Whenever a physical mechanism leads to a cosmic background in some energy band, the best quantity to characterise it is the angular power spectrum C_l, in particular its anisotropic component (APSAC). Indeed, precious informations are concealed within the APSAC, as in the case, e.g., of the temperature anisotropies of the CMB which have been precisely measured with Plank's observations [8].
In this section we will construct a general expression for the APSAC, relative to a radiation generating a cosmic background. To achieve this, two quantities must first be introduced: The power spectrum of the matter distribution $P(k)$ and the intensity of the radiation I_γ. We will start by defining the former.

3.1.1 Power Spectrum $P(k)$

The power spectrum $P(k)$ accounts for the distribution of matter in the Universe and is defined as the Fourier transform of the matter correlation function $\xi(r)$ [68]. This last quantity, also referred to as the *two-point* or *autocorrelation* function, expresses the excess probability, with respect to a random distribution of matter, of finding two mass elements with the same features in volumes dV_1 at $\vec{x}_1$ and in dV_2 at $\vec{x}_2$, thus separated by $r = |\vec{x}_1 - \vec{x}_2|$.

Introducing the *density contrast*, defined as

$$\delta(\vec{r}) = \frac{\rho(\vec{r}) - \langle\rho\rangle}{\langle\rho\rangle}$$

where ρ is the matter energy density and $\langle\rho\rangle$ is its mean value in the Universe, the correlation function is given by

$$\begin{aligned}\xi(|\vec{x}_1 - \vec{x}_2|) &= \langle\delta(\vec{x}_1)\delta(\vec{x}_2)\rangle \\ &= \int \frac{d^3\vec{k}_1\, d^3\vec{k}_2}{(2\pi)^6} \left\langle \tilde{\delta}(\vec{k}_1)\tilde{\delta}(-\vec{k}_2)\right\rangle e^{-(i\vec{k}_1\cdot\vec{x}_1 - i\vec{k}_2\cdot\vec{x}_2)} \,,\end{aligned} \tag{3.1.1}$$

where in the second line we have taken the Fourier transform of $\delta(\vec{x})$ and performed the change of variable $\vec{k}_2 \to -\vec{k}_2$. In this way the product inside the integral becomes

$$\tilde{\delta}(\vec{k}_1)\tilde{\delta}(-\vec{k}_2) = \tilde{\delta}(\vec{k}_1)\tilde{\delta}^*(\vec{k}_2) \,,$$

being $\delta(\vec{x})$ a real-valued function. We can now define the power spectrum $P(k)$ as

$$\left\langle \tilde{\delta}(\vec{k}_1)\tilde{\delta}^*(\vec{k}_2)\right\rangle = (2\pi)^3\, P(\vec{k}_1)\, \delta^3(\vec{k}_1 - \vec{k}_2) \,, \tag{3.1.2}$$

where δ^3 is the 3-dimensional Dirac delta. Inserting this last expression into Eq. 3.1.1, we obtain

$$\xi(r) = \int \frac{d^3\vec{k}}{(2\pi)^3}\, P(k)\, e^{-i\vec{k}\cdot\vec{r}} \,,$$

from where we can see that $P(k)$ is the Fourier transform of $\xi(r)$ [68]. It is worth noting that, since we have introduced $\delta(\vec{x})$ as a random field, the spatial mean $\langle\ \rangle$ can correspond to an *ensemble average* under the assumption of *ergodicity*. For clarity, we remind the formulation of the ergodic hypothesis: ensemble averages equal spatial averages when taken over a realisation of a random field.

Since the distribution of DM in the Universe cannot be directly surveyed, $P(k)$ needs to be evaluated by different means than the one just presented. In this situation, the *halo model* provides a powerful tool to estimate $P(k)$ for DM [67].
The halo model allows to construct the *cosmological mass function*, $n(M, z)dM$ [69], which gives the number density of DMHs at redshift z, in unit of mass M. Combining it with the DM density profiles inferred from N-body simulations [70], we can reconstruct the distribution of DM in the Universe. From this we can build an expression for $P(k)$, which will be the sum of two terms: 1-halo and 2-halo terms, the former giving the contribution from two mass elements within the same halo and the latter from two mass elements contained in two distinct halos. The corresponding formulas are

$$P(k) = P^{1\mathrm{h}}(k) + P^{2\mathrm{h}}(k) \tag{3.1.3}$$

with

$$P^{1\mathrm{h}}(k) = \int dM\, n(M) \left(\frac{M}{\Omega_{\mathrm{M}}\, \rho_{\mathrm{cr}}}\right)^2 |u(k|M)|^2 \tag{3.1.4}$$

$$P^{2\mathrm{h}}(k) = \left[\int dM\, n(M) \left(\frac{M}{\Omega_{\mathrm{M}}\, \rho_{\mathrm{cr}}}\right) b(M)\, |u(k|M)|\right]^2 \times P_{\mathrm{lin}}(k) \tag{3.1.5}$$

where

- $u(k|M)$ is related to $\rho_{\rm DM}(r)$ by the following transformation

$$u(\mathbf{k}|M) = \frac{\int d^3\mathbf{k}\, \rho_{DM}(\mathbf{x}|M)\, e^{-i\mathbf{k}\cdot\mathbf{x}}}{\int d^3\mathbf{k}\, \rho_{DM}(\mathbf{x}|M)}$$

- $b(M)$ is the linear bias, i.e. the parameter which quantifies the relationship between the spatial distribution of galaxies and the underlying dark matter density field [67]

- $P_{\rm lin}(k)$ is the linear power spectrum of density perturbations [1]

The power spectrum is defined in Eq. 3.1.4 and 3.1.5 to be proportional to the first power of the DM density profile $\rho_{DM}(r)$. This is motivated by the considered process: in a decay the signal intensity is proportional to the column density of the radiating source, $\int \rho_{DM}(r)\, dr$, i.e. the integral of the DM distribution along the line-of-sight ($l.o.s$). As a result, the corresponding $P(k)$ will be proportional to the first power of $\delta(z, \vec{r})$. In the case of DM annihilation [71], instead, the signal intensity is proportional to $\int \rho^2_{DM}(r)\, dr$ because of kinematical considerations, resulting in a $P(k)$ proportional to the density contrast squared.

3.1.2 Intensity I_γ

In astrophysics, the intensity of the radiation coming from a source is given as the *surface brightness* per unit photon energy E_γ which, in turn, is defined as

$$\text{Surface Brightness} = \frac{\text{flux density}}{\text{unit solid angle}}$$

where, to calculate the *flux density*, we first need to define the emitting volume.
Given a source of radius R_0, seen in a solid angle $d\Omega$ with extesion dr at redshift z, its observed volume is

$$V = (R_0\, S_k(r))^2\, R_0\, dr\, d\Omega\, (1+z)^{-3}$$

where $S_k(r)$ accounts for spacetime geometry. This volume will produce the luminosity L_γ, given by

$$L_\gamma = V\, \epsilon_\gamma$$

where ϵ_γ is the *volume emissivity*, defined as the energy of photons in unit volume, time and energy range. From L_γ we obtain the observed flux density as

$$\begin{aligned}\mathcal{F}_\gamma &= \frac{L_\gamma}{4\pi\ (R_0\, S_k(r))^2\, (1+z)} \\ &= \epsilon_\gamma \frac{R_0\, dr\, d\Omega}{4\pi\ (1+z)^4}\ .\end{aligned}$$

The intensity I_γ is then the $l.o.s$ integral of $\mathcal{F}_\gamma$ in unit of solid angle and photon energy E_γ, i.e.

$$\begin{aligned}I_\gamma(E_\gamma) &= \frac{1}{4\pi} \int_{l.o.s} \frac{\epsilon_\gamma\, dr\, R_0}{E_\gamma\, (1+z)^4} \\ &= \frac{c}{4\pi} \int \frac{\epsilon_\gamma\, dz}{E_\gamma\, H(z)\, (1+z)^4}\end{aligned} \tag{3.1.6}$$

where in the second line we changed the integration variable from comoving distance r to redshift z, according to the following transformation

$$dr = \frac{c\,dz}{H(z)} \tag{3.1.7}$$

with c the vacuum speed of light and $H(z)$ the Hubble function.

Averaging Eq. 3.1.6 over all directions in the sky we obtain the mean isotropic intensity $\langle I_\gamma(E_\gamma)\rangle$, from which we can express the anisotropic component of the emission as

$$\delta I_\gamma = I_\gamma - \langle I_\gamma \rangle$$

which can then be expanded into spherical harmonics

$$\delta I_\gamma = \langle I_\gamma \rangle \sum_{l,m} a_{lm} Y_{lm}(\hat{n}) \ .$$

This last relation can be inverted making use of the orthogonality of spherical harmonics, which is expressed as

$$\int_{\theta=0}^{\pi} \int_{\phi=0}^{2\pi} sin\ \theta\ d\theta\ d\phi\ Y_{l'm'}(\hat{n})\ Y^{\dagger}_{lm}(\hat{n}) = \delta_{l\,l'}\ \delta_{m\,m'}\ , \tag{3.1.8}$$

thus giving

$$\langle I_\gamma \rangle\ a_{l',m'} = \int d\hat{n} Y^{\dagger}_{l'm'}(\hat{n})\ \delta I_\gamma \ .$$

Finally the *angular power spectrum* is, by definition, given by

$$C_l = \left\langle |a_{l,m}|^2 \right\rangle \ . \tag{3.1.9}$$

3.2 Galactic foreground vs Extragalactic component

When performing measurements of cosmic backgrounds in any energy band of the electromagnetic spectrum, it is common practice to evaluate also the Galactic foreground emission and then subtract it from the observations. The reason for doing so is that our galaxy hosts astrophysical sources which emit in the energy band in exam, thus inevitably contaminating the measurements. Recalling the target of this project - predict the ν_s decay anisotropy pattern in the CXB - the intensity of photons resulting from ν_s decaying within the DMH of the MW will be evaluated and compared to the extragalactic mean component.
The photon flux corresponding to such process (and similarly for annihilation [72]) is given by

$$\Phi(E_\gamma, \psi) = P(E_\gamma) \times J(\psi) \ . \tag{3.2.1}$$

Here $P(E_\gamma)$ is the factor which incorporates all the particle physics features of the considered DM candidate, whereas all astrophysical aspects of the process are contained in

$J(\psi)$ [72]. This astrophysical factor consists of the *l.o.s* integral of the DM distribution along the direction of observation, averaged over all directions, i.e.

$$J(\psi) = \frac{1}{4\pi} \int_{l.o.s.} ds\, \rho_{\rm halo}[r(s,\psi)] \tag{3.2.2}$$

where $\rho_{\rm halo}$ denotes the density distribution of DM particles within the considered DMH as a function of the galactocentric distance r. This, in turn, is parametrized as a function of the *l.o.s* coordinate s and the observation angle ψ [72] in the following way

$$r(s,\psi) = \sqrt{s^2 + R_\odot^2 - 2\, s\, R_\odot\, cos\, \psi} \tag{3.2.3}$$

with $R_\odot = 8.5$ kpc (1 kpc $= 3.08567758 \times 10^{21}$ cm) being the distance of the Sun from the Galactic centre and $cos\, \psi = cos\, b\, cos\, l$, where b and l are the Galactic latitude and longitude, respectively. Although DMHs have no sharp edges, we will adopt an integration range where the upper limit is dictated by the size of the considered halo, i.e. the MW DMH. The limits of integration are then given by

$$s_{\rm min} = 0 \quad , \quad s_{\rm max} = R_\odot\, cos\, \psi + \sqrt{R_{\rm MWH}^2 - R_\odot^2\, sin\, \psi}$$

where $R_{\rm MWH}$ is the radius of the MW DMH, which we will assume to be 100 kpc [73].

3.3 Cross correlation

Angular power spectra can be generally written in the following form [1]

$$C_l^{\rm i,j} = \int \frac{dr}{r^2}\, W^{\rm i}([1+z]E_\gamma, z)\, W^{\rm j}([1+z]E_\gamma, z)\, P\left(\frac{l}{r}, z\right)$$

where $P(l/r, z)$ is the power spectrum (cf. Section 3.1.1) and $W(E, z)$ is the *window function* which, similarly to $P(E_\gamma)$ in Eq. 3.2.1, contains the Particle Physics information related to the particle and the process responsible for the observed radiation. The superscripts 'i,j' refer to two (possibly distinct) radiative mechanisms or considered energies. This feature allows to construct another common quantity to study the angular power spectrum of some cosmic background: The *cross-correlation*, defined as

$$C_l^X = C_l^{1,1} + C_l^{2,2} - 2\, C_l^{1,2}\ . \tag{3.3.1}$$

By evaluating the above expression adopting two different window functions, relative to two different processes, it is possible to evidence the existence of a correlation between the emissions. An example of this procedure is available in Ref. [71], where the DM annihilation signal is cross-correlated with the angular power spectrum of blazars. Equivalently, Eq. 3.3.1 can be computed for the same process, i.e. for the same W, but with each window function evaluated at a different energy. This, instead, allows to probe the correlation between different values of E_γ^1 and E_γ^2.

Chapter 4

Anisotropy Angular Power Spectrum

Having introduced in the previous chapter the techniques and the quantities that will be employed to characterise the CXB, we will now evaluate them in the specific case of a decaying ν_s. This means that, from this point onward, the original results of this project will be presented.
In this chapter we will focus on the APSAC, starting from its detailed derivation, based on the definition of intensity introduced in Section 3.1.2, to the construction of the predictions for its shape in relation to the sensitivity of two future X-ray observatories: the eROSITA and Astro-H space telescopes.

4.1 Intensity and Emissivity

Let us express the intensity of the radiation with energy E_γ, coming from a diffuse source situated along the direction $\hat{n}$ and taking into account the cosmological redshift of photons, as in [1], i.e.

$$I_\gamma(E_\gamma, \hat{n}) = \frac{c}{4\pi} \int dz \frac{\epsilon_\gamma([1+z]E_\gamma, z, \hat{n})}{E_\gamma \, H(z) \, (1+z)^4} \, . \tag{4.1.1}$$

Since the ν_s decay has never been considered before in terms of diffuse emission but only as photon flux from astrophysical objects, no adequate expression for ϵ_γ was available in the literature. Therefore, the following step consists in formulating a suitable expression for this quantity, consistent with its units (photon energy per unit volume, time and energy range). The emissivity of the ν_s decay process that we propose is the following

$$\epsilon_\gamma(E_\gamma, z, \hat{n}r) = E_\gamma \, \frac{dN_\gamma}{dE_\gamma} \Gamma_s \frac{\rho_s(z, \hat{n}r)}{m_s} \tag{4.1.2}$$

where:

- E_γ is the photon energy,
- $\frac{dN_\gamma}{dE_\gamma}$ is the decay spectrum of ν_s, as given in Eq. 2.2.2,
- Γ_s is the decay rate, as given in Eq. 2.2.3,

- $\rho_s(z, \hat{n}r)$ is the energy density of ν_s at redshift z and position $\hat{n}r$.

Eq. 4.1.2 can be rewritten utilising the following quantities

- density parameter of DM

$$\Omega_{\rm DM}(z) = \frac{\langle \rho_{\rm DM}(z) \rangle}{\rho_{\rm cr}(z)} \longrightarrow \Omega_{\rm DM,0} = \frac{\langle \rho_{\rm DM,0} \rangle}{\rho_{\rm cr,0}} = \frac{\langle \rho_{\rm DM}(z) \rangle \ (1+z)^{-3}}{\rho_{\rm cr,0}} \tag{4.1.3}$$

  where we have used of the scaling relation of the matter energy density as a function of redshift, $\rho_{\rm M}(z) \propto (1+z)^3$ [1]; $\rho_{\rm cr}$ is the critical density of the Universe and the subscript 0 on the above quantities indicates their current value, e.g. [8]

$$\rho_{\rm cr,0} = 4.8926 \text{ keV cm}^{-3} ,$$

- density contrast

$$\delta(z, \hat{n}r) = \frac{\rho(z, \hat{n}r) - \langle \rho(z) \rangle}{\langle \rho(z) \rangle} . \tag{4.1.4}$$

Combining these two, the energy density of ν_s in Eq. 4.1.2 can be written as

$$\rho(z, \hat{n}r) = \rho_{cr,0} \, \Omega_{\rm DM,0} \, (1+z)^3 \ [\delta(z, \hat{n}r) + 1] \ ,$$

hence the emissivity becomes

$$\epsilon_\gamma([1+z]E_\gamma, z, \hat{n}r) = E_\gamma \left. \frac{dN_\gamma}{dE'_\gamma} \right|_{E'_\gamma = [1+z]E_\gamma} \Gamma_{\nu_{\rm s}} \, \frac{\rho_{\rm cr,0} \, \Omega_{\rm DM,0}}{m_{\rm s}} \, [\delta(z, \hat{n}r) + 1] \, (1+z)^4 . \tag{4.1.5}$$

Inserting the above expression in Eq. 4.1.1, we obtain the final expression for the intensity of the radiation with energy E_γ coming from a direction $\hat{n}$, resulting from the $\nu_{\rm s}$ decay

$$I_\gamma(E_\gamma, \hat{n}) = c \int \frac{dz}{H(z)} W([1+z]E_\gamma) \, [\delta(z, \hat{n}r) + 1] \tag{4.1.6}$$

where we have introduced the window function $W(E_\gamma)$ (cf. Section 3.3), corresponding to

$$W([1+z]E_\gamma) = \left. \frac{dN_\gamma}{dE'_\gamma} \right|_{E'_\gamma = [1+z]E_\gamma} \frac{\Gamma_{\rm s}}{4\pi} \, \frac{\rho_{\rm cr,0} \, \Omega_{\rm DM,0}}{m_{\rm s}} . \tag{4.1.7}$$

Replacing in Eq. 4.1.7 the expressions for the decay spectrum with Eq. 2.2.2 and the decay rate with Eq. 2.2.3, the window function becomes

$$W([1+z]E_\gamma) = \delta\left([1+z]E_\gamma - \frac{m_{\rm s}}{2}\right) \, 5.5 \times 10^{-22} \theta_{\rm as}^2 \, s^{-1} \, \frac{\rho_{\rm cr,0} \, \Omega_{\rm DM,0}}{4\pi} \left(\frac{m_{\rm s}}{\rm keV}\right)^4 \tag{4.1.8}$$

where we have not replaced the subscript of the DM density parameter ($\Omega_{\rm DM,0}$) from 'DM' to 's'. This choice is the manifestation of the assumption that all dark matter in the Universe is in the form of ν_s, i.e. $\Omega_{\rm s} = \Omega_{\rm DM,0}$.

4.2 Mean Intensity and Anisotropy

As outlined in Section 3.1.2, in order to obtain the mean isotropic component of the CXB, we must now average Eq. 4.1.5 over all directions of observation. However, since $\delta(z, \hat{n}r)$ was introduced as the realisation of a random field, the spatial mean $\langle\,\rangle$ can be replaced by an *ensemble average* over all possible realisations of δ. From Eq. 4.1.3 we immediately see that

$$\langle \delta(z, \hat{n}r) \rangle = 0 \; .$$

So performing the ensemble average of Eq. 4.1.5 evidences the usefulness of having introduced the window function W, because the mean isotropic component of I_γ simply becomes

$$\begin{aligned} \langle I_\gamma(E_\gamma) \rangle &= c \int \frac{dz}{H(z)} W([1+z]E_\gamma) \\ &= c\, 5.5 \times 10^{-22} \theta_{\rm as}^2 \; s^{-1} \; \frac{\rho_{\rm cr,0}\, \Omega_{\rm DM,0}}{4\pi \; {\rm keV}} \left(\frac{m_{\rm s}}{\rm keV}\right)^4 \int dz \frac{\delta\left([1+z]E_\gamma - \frac{m_{\rm s}}{2}\right)}{H(z)} \\ &= c\, P(m_{\rm s}, \theta_{\rm as}^2) \; \frac{\rho_{\rm cr,0}\, \Omega_{\rm DM,0}}{4\pi \; {\rm keV}} \; \frac{1}{E_\gamma \, H(\frac{m_{\rm s}}{2\, E_\gamma} - 1)} \end{aligned} \tag{4.2.1}$$

which as units of $[{\rm keV}^{-1}{\rm s}^{-1}{\rm cm}^{-2}{\rm sr}^{-1}]$ and where $P(m_{\rm s}, \theta_{\rm as}^2)$ represents the factor collecting all mixing parameters of the ν_s, i.e.

$$P(m_{\rm s}, \theta_{\rm as}^2) = 5.5 \times 10^{-22} \, \theta_{\rm as}^2 \; s^{-1} \; \left(\frac{m_{\rm s}}{\rm keV}\right)^4 \; . \tag{4.2.2}$$

It is important to highlight that $\nu_{\rm s}$ decaying at high redshift will also contribute to the intensity of the radiation and, thus, to the mean isotropic component as well as the APSAC of the CXB. This feature manifests itself as a redshift correction in the photon's energy within the $\nu_{\rm s}$ decay spectrum, i.e. the $[1+z]$ factor in front of E_γ in Eq. 4.2.1. The plot in Fig. 4.1 shows $\langle I(E_\gamma) \rangle$ multiplied by E_γ^2 as a function of the energy E_γ. Here we can identify all the features already presented at the end of Sec. 2.2.2, i.e. the peak at $\sim m_{\rm s}/2$, the broadening at slightly higher energies due to σ_v and the non-negligible contribution from $E_\gamma < m_{\rm s}/2$ due to high-redshift decaying $\nu_{\rm s}$.

Now, in a similar fashion to Section 3.1.2, we calculate the deviation from this mean value

$$\begin{aligned} \delta I_\gamma &= I_\gamma - \langle I_\gamma \rangle \\ &= \int dr \; W([1+z]E_\gamma) \; [(\delta(z, \hat{n}r) + 1) - 1] \end{aligned} \tag{4.2.3}$$

and then expand it in spherical harmonics

$$\delta I_\gamma = \langle I_\gamma \rangle \sum_{l,m} a_{l\,m} Y_{l\,m}(\hat{n}) \; . \tag{4.2.4}$$

Using the orthogonality of spherical harmonics (cf. Eq. 3.1.8), this last relation can be inverted to obtain

$$\langle I_\gamma \rangle \; a_{l,m} = \int d\hat{n} Y_{l\,m}^\dagger(\hat{n}) \, \delta I_\gamma \; . \tag{4.2.5}$$

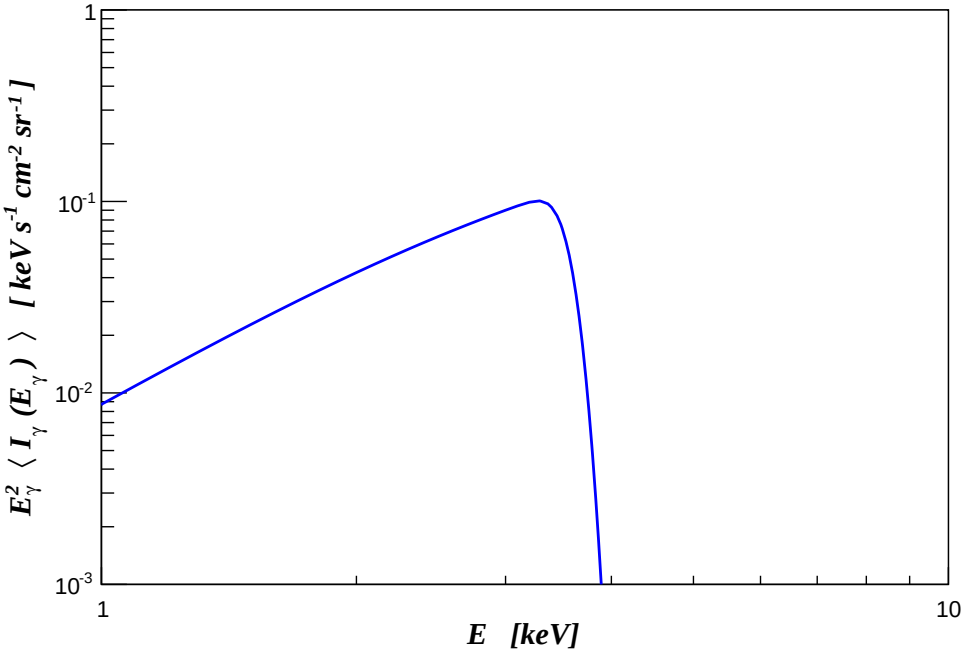

Figure 4.1: Mean isotropic intensity (Eq. 4.2.1) multiplied by the photon energy squared to highlight the contribution from high-redshift decaying ν_s. The considered mass is $m_s = 7.1$ keV

After inserting Eq. 4.2.3 in the above expression, we obtain

$$\langle I_\gamma \rangle \; a_{l,m} = \int dr \int d\hat{n} \; Y^\dagger_{l\,m}(\hat{n}) \; \delta(z, \hat{n}r) \; W([1+z]E_\gamma) \; . \tag{4.2.6}$$

We now replace $\delta(z, \hat{n}r)$ with its Fourier expansion

$$\langle I_\gamma \rangle \; a_{l,m} = \int dr \int d\hat{n} \; Y^\dagger_{l\,m}(\hat{n}) \; W([1+z]E_\gamma) \int \frac{d\vec{k}}{(2\pi)^3} \; e^{i\vec{k}\cdot\vec{r}} \; \tilde{\delta}(z, \vec{k}) \tag{4.2.7}$$

and expand the exponential term using the Rayleigh equation, which reads

$$e^{i\vec{k}\cdot\vec{r}} = 4\pi \sum_{l=0}^{\infty} \sum_{m=-l}^{l} \; i^l \; Y_{l\,m}(\hat{r}) \; Y^\dagger_{l\,m}(\hat{k}) \; j_l(kr) \; ,$$

where $j_l(k\,r)$ is the spherical Bessel function of order l. With this Eq. 4.2.7 becomes

$$\langle I_\gamma \rangle \; a_{l,m} = \int dr \int d\hat{n} Y^\dagger_{l\,m}(\hat{n}) W([1+z]E_\gamma) \int \frac{d\vec{k}}{(2\pi)^3} \tilde{\delta}(z, \vec{k}) 4\pi \sum_{l',m'} i^{l'} \, j_{l'}(kr) Y^\dagger_{l'\,m'}(\hat{k}) Y_{l'm'}(\hat{n}) \; . \tag{4.2.8}$$

Making use of the orthogonality once more, we arrive at

$$\langle I_\gamma \rangle \; a_{l,m} = i^l \int dr \int \frac{d\vec{k}}{2\pi^2} \; W([1+z]E_\gamma) \; j_l(k\,r) \; Y^\dagger_{l\,m}(\hat{k}) \; \tilde{\delta}(z, \vec{k}) \; . \tag{4.2.9}$$

In order to derive an expression for the APSAC as in Eq. 3.1.9, we need to multiply this last result by its complex conjugate and then take the ensemble average $\langle \, \rangle$ once again, i.e.

$$C_l(E_\gamma) = \langle I_\gamma \rangle^2 \; \left\langle |a_{l,m}|^2 \right\rangle$$

which leads to

$$C_l(E_\gamma) = \int dr \int dr' \int \frac{d\vec{k}}{2\pi^2} \int \frac{d\vec{k'}}{2\pi^2} W([1+z]E_\gamma)^2 \times \\ \times j_l(k\,r)\, j_l(k'\,r')\, Y^\dagger_{l\,m}(\hat{k})\, Y_{l\,m}(\hat{k'}) \left\langle \tilde{\delta}(z,\vec{k})\, \tilde{\delta}^*(z,\vec{k'}) \right\rangle \,. \quad (4.2.10)$$

In the last line we can recognise the definition of power spectrum from Eq. 3.1.2 which, upon substitution inside Eq. 4.2.10, both removes the integral over $d\vec{k'}$ and, eventually, introduces $P(k)$ into this derivation

$$C_l(E_\gamma) = \int dr \int dr' \int d\vec{k}\, \frac{2}{\pi} W([1+z]E_\gamma)^2 \times \\ \times j_l(k\,r)\, j_l(k\,r')\, Y^\dagger_{l\,m}(\hat{k})\, Y_{l\,m}(\hat{k})\, P_\delta(k) \quad (4.2.11)$$

where the subscript δ in $P(k)$ indicates that this power spectrum is obtained from the first power of the matter density distribution, as discussed at the bottom of Section 3.1.1. We can use the orthogonality relation once more to further reduce the notation, giving

$$C_l(E_\gamma) = \int dr \int dr' \int dk\, k^2\, \frac{2}{\pi} W([1+z]E_\gamma)^2\, j_l(k\,r)\, j_l(k\,r')\, P_\delta(k) \,. \quad (4.2.12)$$

The final step in this derivation consists in utilising the following approximation

$$\frac{2}{\pi} \int dk\, k^2\, P_\delta(k,r,r')\, j_l(k\,r)\, j_l(k\,r') \approx \frac{1}{r^2}\, P_\delta(k=\frac{l}{r},z)\, \delta(r-r') \,, \quad (4.2.13)$$

which is valid if $P(k;r,r')$ varies relatively slow as a function of k, and it eventually leads to the final expression of the APSAC

$$C_l(E_\gamma) = \int \frac{dr}{r^2}\, W^2([1+z]E_\gamma)\, P_\delta(k=\frac{l}{r},z) \quad (4.2.14)$$

or equivalently, making use of Eq. 3.1.7, expressed as an integral over redshift

$$C_l(E_\gamma) = \int \frac{c\,dz}{H(z)\,r^2(z)}\, W^2([1+z]E_\gamma)\, P_\delta\left(\frac{l}{r(z)},z\right) \,. \quad (4.2.15)$$

The formula above represents one of the main results of this project, namely the APSAC of the ν_s decay in the assumption that the totality of DM in the Universe is in the form of sterile neutrinos. Its units are $(\mathrm{keV}^{-1}\,\mathrm{cm}^{-2}\,\mathrm{s}^{-1}\,\mathrm{sr}^{-1})^2$ and its a function of the photon energy E_γ and the multipole l.
We will now proceed to evaluate it in the next Section.

4.3 Angular Power Spectrum of the Anisotropic Component

In order to obtain predictions for the APSAC of the ν_s decay, we need to compute Eq. 4.2.15 numerically. To achieve this, we need to define a suitable expression for the

square of the Dirac-delta contained in W^2 and a set of values of the power spectrum for different wavenumbers, up to a given redshift $P_\delta(k,z)$. In addition, the latter should be evaluated as prescribed at the end of Section 3.1.1, i.e. as a function of the first power of the matter density distribution. The solution to these issues will have important implications for our results. For this reason we shall proceed in order by first introducing the necessary technical prerequisites and then presenting and commenting our results for all examined scenarios.

4.3.1 Technical Requirements

The most straightforward way to implement the Dirac-delta is by approximating it with a narrow gaussian function

$$\delta\left([1+z]E_\gamma - m_s/2\right) \approx \frac{e^{-\frac{\left([1+z]E_\gamma - m_s/2\right)^2}{\varepsilon^2}}}{\varepsilon\sqrt{\pi}} \tag{4.3.1}$$

centred at $m_s/2$ and with width ε. The latter parameter has an important role when constructing the predictions for the APSAC, as it can be associated with the spectral resolution of the device that will perform the observations.

$P_\delta(k,z)$ can be numerically calculated from Eq. 3.1.4 and 3.1.5 and this can be achieved by utilising, for example, the CAMB code [74]. The latter is engineered to generate, among other quantities, the matter power spectrum values for the desired cosmology, resulting from the evolution of the primordial density perturbations $P_{\rm prim}(k)$ [1]. CAMB can also be set to produce results in both CDM and WDM scenarios. The data sets which have been employed in this project assume a CDM cosmology and had the following characteristics: each set refers to a redshift from $z=0$ to $z=2$ and each contains pairs of wavenumber k and the corresponding $P(k,z)$, with k ranging from $10^{-4}\,\mathrm{Mpc}^{-1}$ up to $10^4\,\mathrm{Mpc}^{-1}$. In Fig. 4.2 the power spectrum values as a function of wavenumber are shown for $P(k,z=0)$ in *red*, $P(k,z=1)$ in *green* and $P(k,z=2)$ in *blue*. We shall remark several key features of this plot: all three curves grow as a power law $P(k)\propto k^n$ with spectral index $n\simeq 1$, up to the wavenumber of equivalence ($k_{\rm eq}\simeq 0.02\,\mathrm{Mpc}^{-1}$); the wiggles at $k\simeq 0.1\,\mathrm{Mpc}^{-1}$ are the manifestations of Baryon Acoustic Oscillations (BAO) [75]; all three curves have a hump at $k>1\ \mathrm{Mpc}^{-1}$ given by the small-scale non-linear effects on matter distribution [1]; finally $P(k,z)$ increases with decreasing z, in agreement with the prediction of matter clustering at low redshift.
The power spectrum values produced via CAMB, however, could not be directly implemented into the numerical code that has been developed to evaluate Eq. 4.2.15. The reason is hidden in the dependency of such formula from the multipole l and in the relation between this quantity with the wavenumber k and the comoving distance $r(z)$, which reads

$$l = k\times r(z)\ . \tag{4.3.2}$$

Hence, in order to adequately employ the available k and $P(k,z)$, we first needed to interpolate them relatively to the desired ls and $r(z)$. The former were not chosen randomly because they consist of integer values associated to the angular resolution θ of the

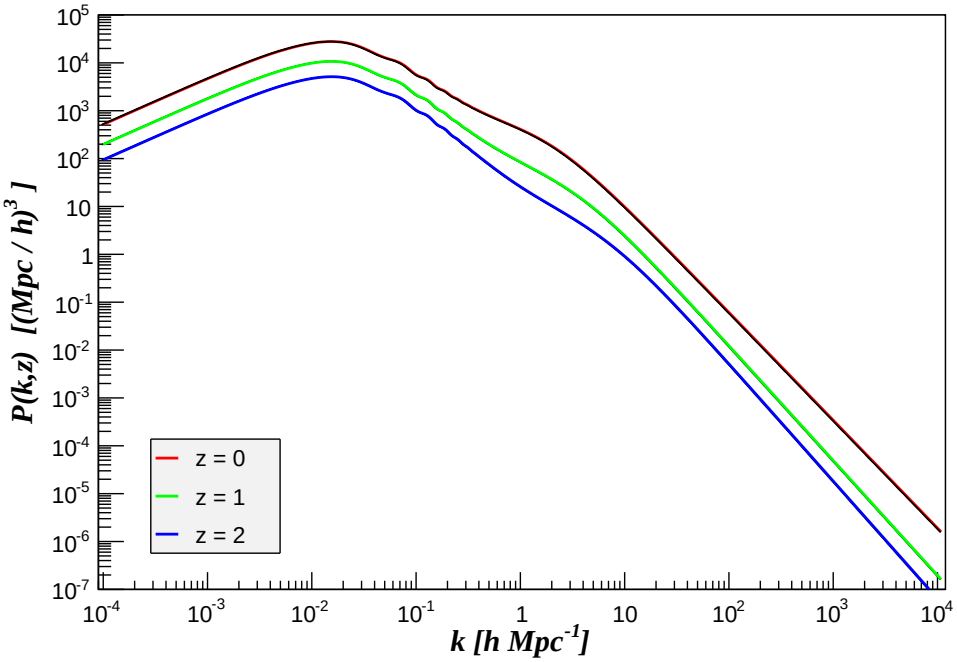

Figure 4.2: Power spectrum $P(k, z)$ of matter density perturbations obtained with CAMB [74] at three different redshifts: $z = 0$ (red curve), $z = 1$ (green curve) and $z = 2$ (blue curve)

device that will perform the observations. Indeed, the maximum multipole l that can be assessed is dictated by θ via

$$l_{\max} \approx \frac{\pi}{\theta} \, . \tag{4.3.3}$$

The values of $r(z)$, instead, were obtained by integrating Eq. 3.1.4 up to the z in consideration, i.e.

$$r(z) = \int_0^z \frac{c \, dz'}{H(z')} \, . \tag{4.3.4}$$

Considering that the redshift range in exam is $[0, 2]$, the relevant contributions to the Hubble function in Eq. 4.3.4 are primarily due to the matter and cosmological constant components. Hence, deeply into the matter-dominated era, we can approximate $H(z) \simeq H_0 \sqrt{\Omega_M \, (1+z)^3 + \Omega_\Lambda}$. The values of the cosmological parameters that have been adopted were obtained from the latest analysis of the CMB [8]: $H_0 = 68.14$ Kms^{-1}Mpc^{-1}, $\Omega_{\mathrm{M},0} = 0.3036$, $\Omega_{\mathrm{DM},0} = 0.2542$ and $\Omega_{\Lambda,0} = 0.6964$.

Before proceeding to the results, it is educative to analyse Eq. 4.2.15 and 4.1.8 in depth. We observe that, along with the cosmological parameters and the two variables E_γ and l, there are two free parameters: m_{s} and θ^2_{as}. However, recalling Eq. 2.2.2, we know that the ν_{s} mass and the photon energy are linked via the decay spectrum ($E_\gamma = m_{\mathrm{s}}/2$), whereas the mixing angle is constrained to the mass via X-ray observations. Altogether, these considerations reduce the number of free parameters in the APSAC.
We conclude by reporting in Table 4.1 the technical specifications of the two instruments on which our predictions are based upon: eROSITA [76] and Astro-H [78].

Table 4.1: Technical specifications of eROSITA [76] and Astro-H [78]

	eROSITA (Soft X-ray)	Astro-H (Soft X-ray)	Astro-H (Hard X-ray)
energy range	0.2-10 keV	0.4-12 keV	5-80 keV
spectral resolution, ε	138 eV	7 eV	< 1.5 keV
angular resolution, θ	~ 25 arsec	~ 1.7 arcmin	~ 1.7 arcmin
maximum multipole, $l_{\max}$	$\sim 23,143$	$\sim 6,353$	$\sim 6,353$
effective FOV, $\Omega_{\rm FOV}$	$\sim 0.83\,\deg^2$	$9\,\mathrm{arcmin}^2$	$\sim 81\,\mathrm{arcmin}^2$
effective area, $\mathrm{A_{eff}}$	$139\,\mathrm{cm}^2$	$360\,\mathrm{cm}^2$	$300\,\mathrm{cm}^2$
covered sky fraction, $\mathrm{f_{sky}}$	1	$1444\,\mathrm{arcmin}^2$	$1444\,\mathrm{arcmin}^2$
background photons, $N_{\rm B}$ $\left[\mathrm{cts\,s^{-1}\,cm^{-2}\,sr^{-1}\,keV^{-1}}\right]$	7.3×10^{-5}	$< 4.8\times10^{-4}$	$< 2.5\times10^{-5}$
exposure time, $t_{\rm exp}$	2548s	40-100 Ks	40-100 Ks

4.3.2 Results: Cold Dark Matter scenario

In this section we present the results for the CXB APSAC resulting from the $\nu_{\rm s}$ decay in the CDM scenario. Considering the likeliness of DM in the form of a keV $\nu_{\rm s}$, a broad range of possible masses in this energy scale is probed. The predictions are organised in the following way: two distinct groups of results have been generated, one forecasting the observations of Astro-H and the other of eROSITA; for each one we consider two different sets of $m_{\rm s}$ values and the corresponding E_γ. As anticipated in Section 2.2.3, the first set comprises two values favoured by recent X-ray observations, i.e. $m_{\rm s} = 5$ and 7.1 keV, whereas the second examines slightly higher energies. i.e. $m_{\rm s} = 10$ and 20 keV. Due to the ability of Astro-H of observing the sky on a wider energy range, in the latter set for this instrument $m_{\rm s} = 40$ keV has also been considered. In each case the highest allowed mixing angle has been adopted, in agreement with the constraints presented in Sec. 2.2.3, while $l_{\max}$ and ε have been set according to the resolutions of the considered device (see Table 4.1). Moreover, in compliance with possible angular resolution peaks of the instrumentation (cf. [76] and [78]), the first group of predictions has been obtained up to $l = 10000$, while up to $l = 100000$ the second.
For each of the classes defined above a distinct plot has been produced, which details are schematically summarised below.

- Fig. 4.3 (Astro-H) and Fig. 4.4 (eROSITA)
  The CXB APSAC shown here correspond to the decay signal of sterile neutrino with $m_{\rm s} = 5$ keV (*red* curve) and 7.1 keV (*black* curve). The values of the mixing angles that have been utilised were $\theta^2_{\rm as} = 1\times10^{-10}$ for the former and $\theta^2_{\rm as} = 2\times10^{-11}$ for the latter. The vertical segments spreading from the second curve correspond to the 1-σ error bars, which treatment will be presented at the end of this chapter.

- Fig. 4.5 (Astro-H) and Fig. 4.6 (eROSITA)
  The CXB APSAC shown here correspond to the decay signal of sterile neutrino with $m_{\rm s} = 10$ keV (*black* curve) and 20 keV (*red* curve). The values of the mixing angles that have been utilised were $\theta^2_{\rm as} = 2\times10^{-12}$ for the former and $\theta^2_{\rm as} = 1\times10^{-13}$ for the latter. The *green* curve in the first figure refers to the $m_{\rm s} = 40$ keV case, for which $\theta^2_{\rm as} = 1\times10^{-14}$ has been set.

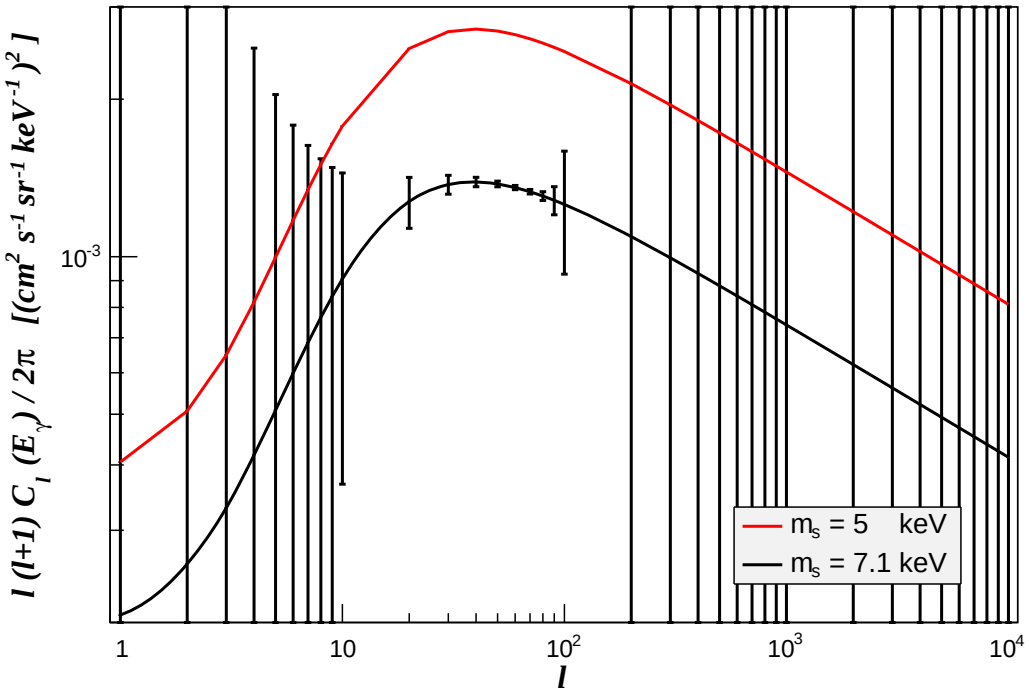

Figure 4.3: APSAC of a decaying CDM sterile neutrino with $m_s = 7.1$ keV (*black curve*) and $m_s = 5$ keV (*red curve*), relative to the sensitivity of Astro-H. The values of the mixing angles are: $\theta^2_{as} = 1 \times 10^{-10}$ for the first and $\theta^2_{as} = 2 \times 10^{-11}$ for the second. The 1-σ errors bars, associated with the first of the two considered energies, are also shown.

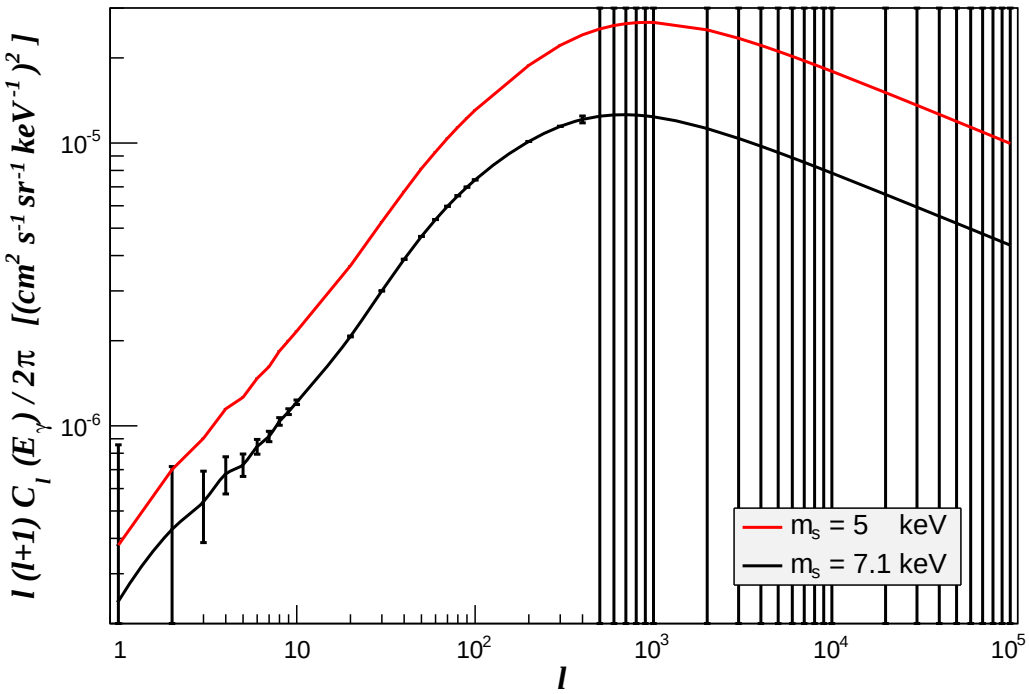

Figure 4.4: APSAC of a decaying CDM sterile neutrino with $m_s = 7.1$ keV (*black curve*) and $m_s = 5$ keV (*red curve*), relative to the sensitivity of eROSITA. The values of the mixing angles are: $\theta^2_{as} = 1 \times 10^{-10}$ for the first and $\theta^2_{as} = 2 \times 10^{-11}$ for the second. The 1-σ errors bars, associated to the first of the two considered energies, are also shown.

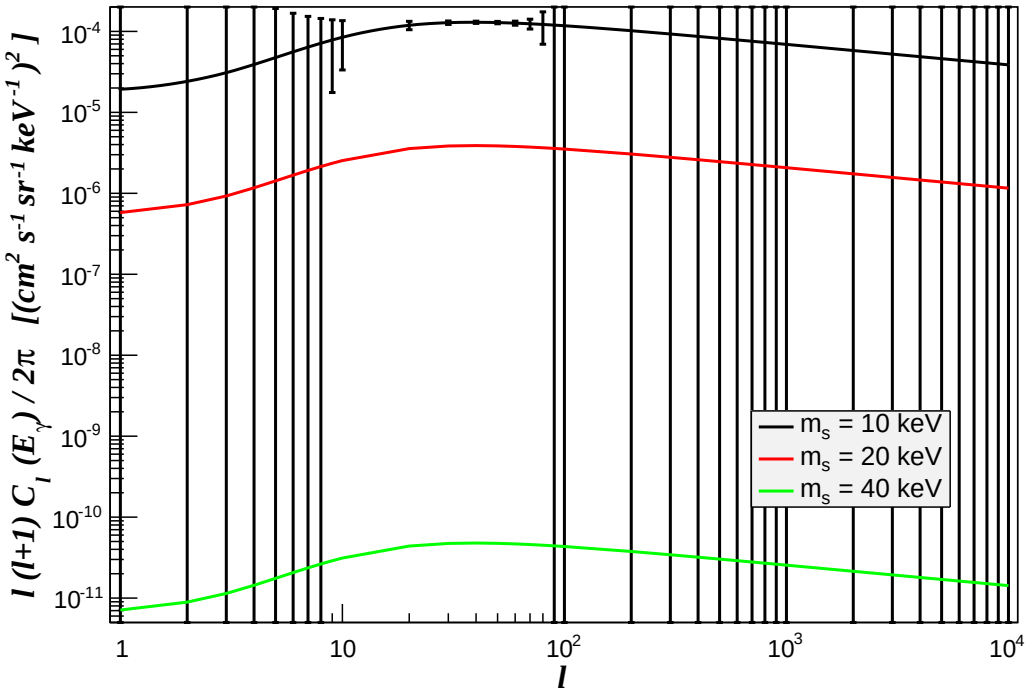

Figure 4.5: APSAC of a CDM ν_s decay relative to the sensitivity of Astro-H. Each curve corresponds to following couples of $(m_s\,,\theta^2_{as})$ values: (10 keV - 2 $\times 10^{-12}$) in *black*, (20 keV - 1 $\times 10^{-13}$) in *red* and (40 keV - 1 $\times 10^{-14}$) in *green*. The 1-σ errors bars, associated to the first of the above energies, are also shown.

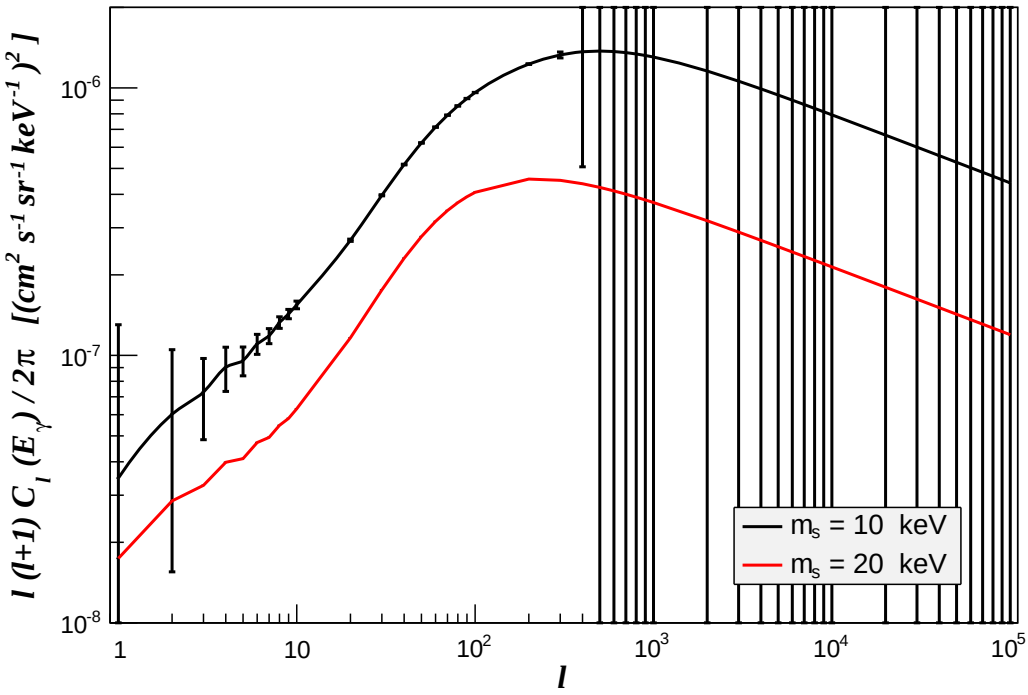

Figure 4.6: APSAC of a decaying CDM sterile neutrino with m_s = 10 keV (*black* curve) and m_s = 20 keV (*red* curve), relative to the sensitivity of eROSITA. The values of the mixing angles are: $\theta^2_{as} = 2\times10^{-12}$ for the first and $\theta^2_{as} = 1\times10^{-13}$ for the second. The 1-σ errors bars, associated to the first of the two considered energies, are also shown.

Due to the lack of updated X-ray upper bounds in the range $m_{\rm s} \gtrsim 10$ keV, the mixing angles that have been adopted at higher masses were conservative values obtained by extrapolating the available constraints, i.e. those shown in Fig. 2.3.

There are several interesting features in the plots above that is important to underline. When comparing Fig. 4.3 with 4.4, and similarly Fig. 4.5 with 4.6, two remarkable differences emerge: the approximately three oders of magnitude higher intensities detected by Astro-H and the greater raggedness of the curves predicted for eROSITA, both of which are evident especially at low l. These differences are both attributable to the greater spectral resolution of Astro-H in the Soft X-ray band, since a smaller ε leads to more power observed on each angular scale. This situation is well depicted in Fig. 4.7 where the black curves of Fig. 4.3 and 4.4 are shown together for comparison. Notice how the prediction for eROSITA (*black* curve) in the range $l = [10, 10^5]$ resembles that of Astro-H (*red* curve) in the range $l = [1, 10^4]$, thus confirming what stated above.
The greater smoothness of the predictions for Astro-H can be seen as a drawback because the wiggles at $3 \leq l \leq 9$, visible in Fig. 4.4 and 4.6 for eROSITA, contain considerable physical information. Recalling the dependence of the APSAC from $P(k, z)$, expressed in Eq. 4.2.15, we can identify several power spectrum features into these plots. Among the most noticeable, the irregularities at $l < 10$ can be related to the BAO visible at $k \sim 0.1\,\mathrm{Mpc}^{-1}$ in Fig. 4.2, and the change of tilt at $l \sim 50$ which, in turn, can be associated to a similar change at $k \sim 1\,\mathrm{Mpc}^{-1}$ in the same figure, due to the contribution of non-linear effects on the matter power spectrum.
Another important feature, which is particularly evident in Fig. 4.5, is the non trivial dependence of the APSAC from $m_{\rm s}$ and $\theta^2_{\rm as}$. The reason for this behaviour can be traced to the non-linear dependence of the photon mean intensity from E_γ and the $\nu_{\rm s}$ mass and mixing angle with active neutrinos. Examining Eq. 4.2.1 and 4.2.2, we notice that

$$\langle I_\gamma \rangle \propto \frac{1}{E_\gamma}\, m_{\rm s}^4\, \theta^2_{\rm as} \implies \langle I_\gamma \rangle \propto m_{\rm s}^3\, \theta^2_{\rm as}\ ,$$

and, whereas $m_{\rm s}$ increases of units or of a factor 10 utmost, $\theta^2_{\rm as}$ decreases of several orders of magnitude at each different combination of such values. Therefore, between the two parameters, we can assert that the mixing angle with active neutrinos is the one predominantly controlling the order of magnitude of the APSAC.

4.3.3 Results: Warm Dark Matter scenario

As already explained in Section 4.3.1, the power spectrum data sets which have been utilised throughout this work were obtained via CAMB for a CDM cosmology. However, as previously discussed in Section 2.2.1, the $\nu_{\rm s}$ can be either CDM or WDM, depending on its production mechanism in the Early Universe. Until now, the results presented only referred to a CDM $\nu_{\rm s}$ and, in order to generate predictions for the WDM case, we can either (*i*) generate new adequate power spectrum data by resetting CAMB or (*ii*) adjust the already available values by multiplying them by a *transfer function*.
The second possibility, which we shall pursue for convenience, emerges from N-body simulations performed with WDM. It can be shown [79] that the corresponding matter power spectrum, $P_{\rm WDM}(k)$, can be related to the CDM case, $P_{\rm CDM}(k)$, via a transfer

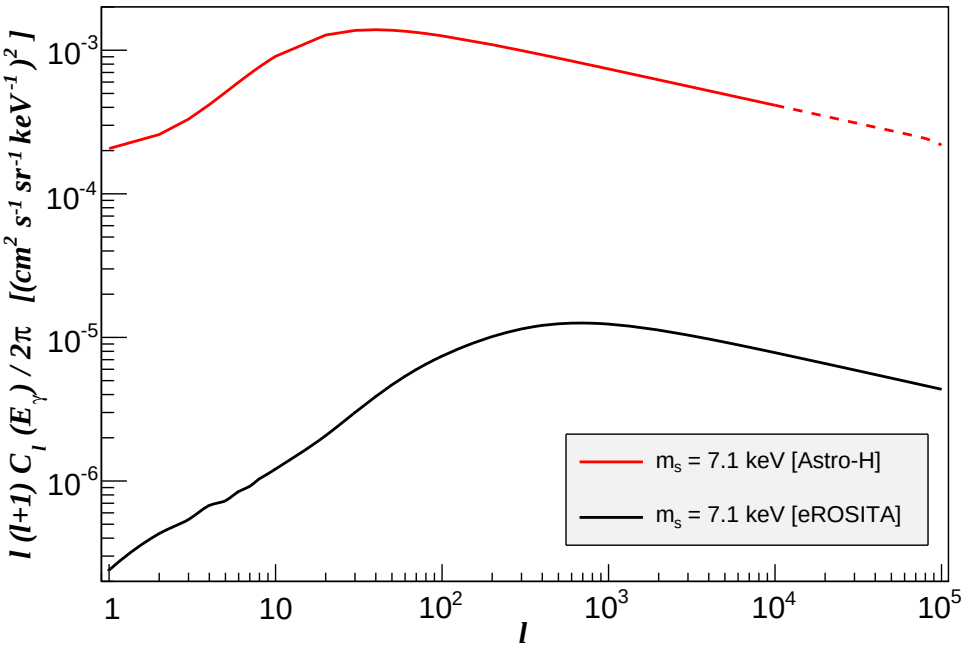

Figure 4.7: Comparison of the APSAC predictions for Astro-H (*red* curve) and eROSITA (*black* curve). The ν_s mass considered is $m_s = 7.1$ keV, with mixing angle $\theta^2_{as} = 2 \times 10^{-11}$.

function $T(k)$. This reads as follows

$$T^2(k) \equiv \frac{P_{\rm WDM}(k)}{P_{\rm CDM}(k)} = [1 + (\alpha\, k)^{\mu\, t}]^{-\frac{s}{\mu}} \ , \tag{4.3.5}$$

where

$$\alpha(m_{\rm WDM}, z) = 0.0476 \left(\frac{1{\rm keV}}{m_{\rm WDM}}\right)^{1.85} \left(\frac{1+z}{2}\right)^{1.3} \ ,$$

and with $\mu = 3$, $t = 0.6$ and $s = 0.4$.
With this expedient, Eq. 4.2.15 becomes

$$C_l^{\rm WDM}(E_\gamma) = \int \frac{c\, dz}{H(z)\, r^2(z)}\, W^2([1+z]E_\gamma)\, P_{\rm CDM}\left(\frac{l}{r(z)}, z\right)\, T^2(k) \ . \tag{4.3.6}$$

The predictions for Eq. 4.3.6 are reported in Fig. 4.8 and 4.9, relatively to Astro-H and eROSITA, respectively. The ν_s mass values, and the corresponding θ^2_{as}, that have been adopted are the same of the first set introduced in the previous subsection, i.e. $m_s = 5, 7.1$ keV.
A quick examination of the Fig. 4.8 and 4.9 evidences how they largely resemble Fig. 4.3 and 4.5. This similarity is evident in Fig. 4.10 and 4.11, where the black curves of Fig. 4.3 and 4.5 (i.e. those for $m_s = 7.1$ keV) are compared to those in Fig. 4.8 and 4.9. In detail, in both plots the *blue* curve corresponds to the CDM case, whereas the *green* one to the WDM scenario. We notice how the two predictions largely overlap over most of the probed multipole range, differing only at the highest l values.

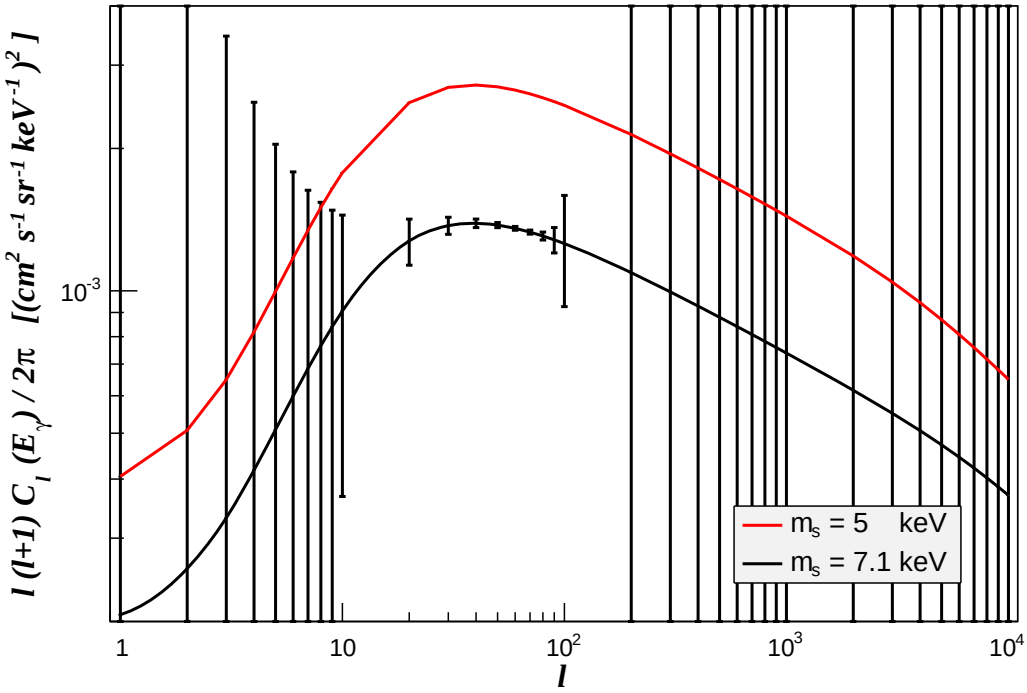

Figure 4.8: APSAC of a decaying WDM sterile neutrino with $m_{\rm s} = 7.1$ keV (*black curve*) and $m_{\rm s} = 5$ keV (*red curve*), relative to the sensitivity of Astro-H. The values of the mixing angles are: $\theta^2_{\rm as} = 1 \times 10^{-10}$ for the first and $\theta^2_{\rm as} = 2 \times 10^{-11}$ for the second. The 1-σ errors bars, associated with the first of the two considered energies, are also shown.

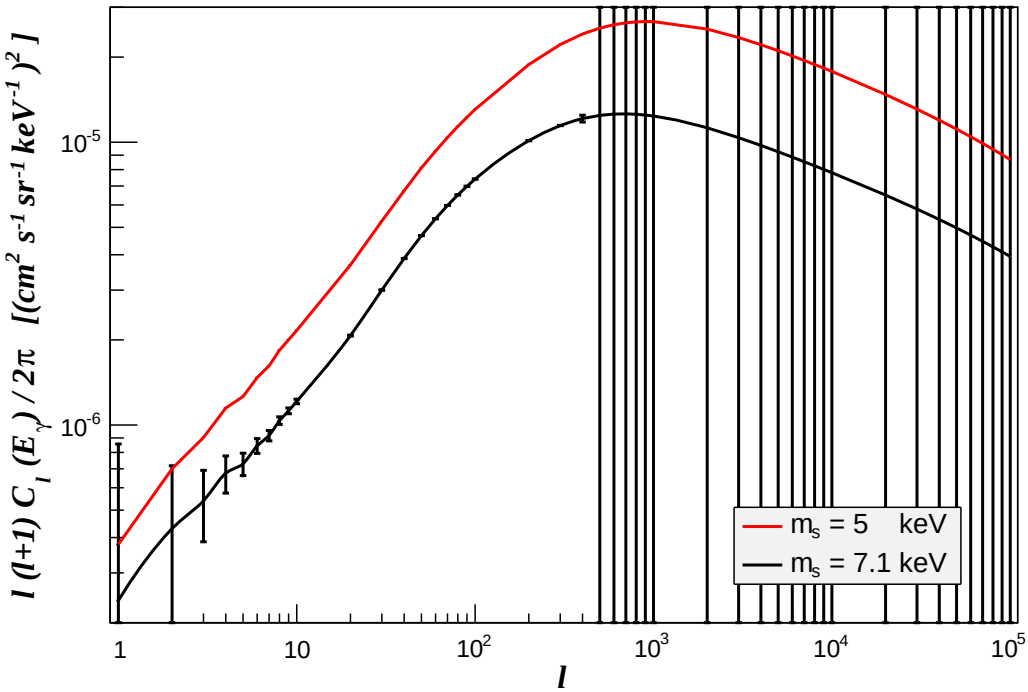

Figure 4.9: APSAC of a decaying WDM sterile neutrino with $m_{\rm s} = 7.1$ keV (*black curve*) and $m_{\rm s} = 5$ keV (*red curve*), relative to the sensitivity of eROSITA. The values of the mixing angles are: $\theta^2_{\rm as} = 1 \times 10^{-10}$ for the first and $\theta^2_{\rm as} = 2 \times 10^{-11}$ for the second. The 1-σ errors bars, associated to the first of the two considered energies, are also shown.

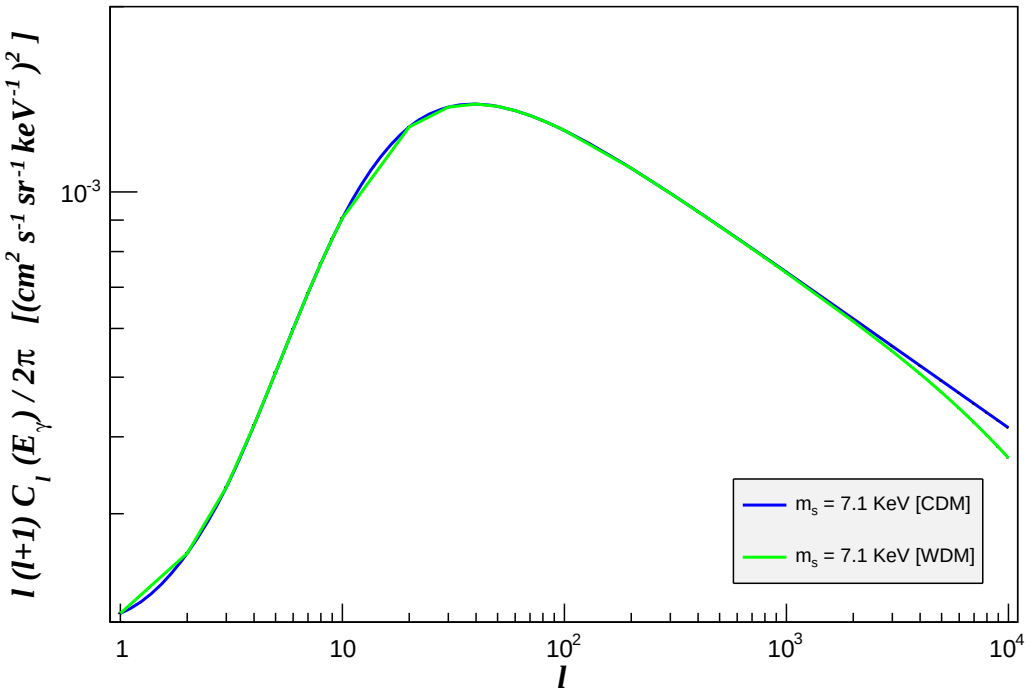

Figure 4.10: Comparison between the APSAC of a decaying CDM (*blue* curve) and a WDM (*green* curve) sterile neutrino with $m_{\rm s} = 7.1$ keV, relative to the sensitivity of Astro-H. The values of the mixing angles are: $\theta^2_{\rm as} = 1 \times 10^{-10}$ for the first and $\theta^2_{\rm as} = 2 \times 10^{-11}$ for the second.

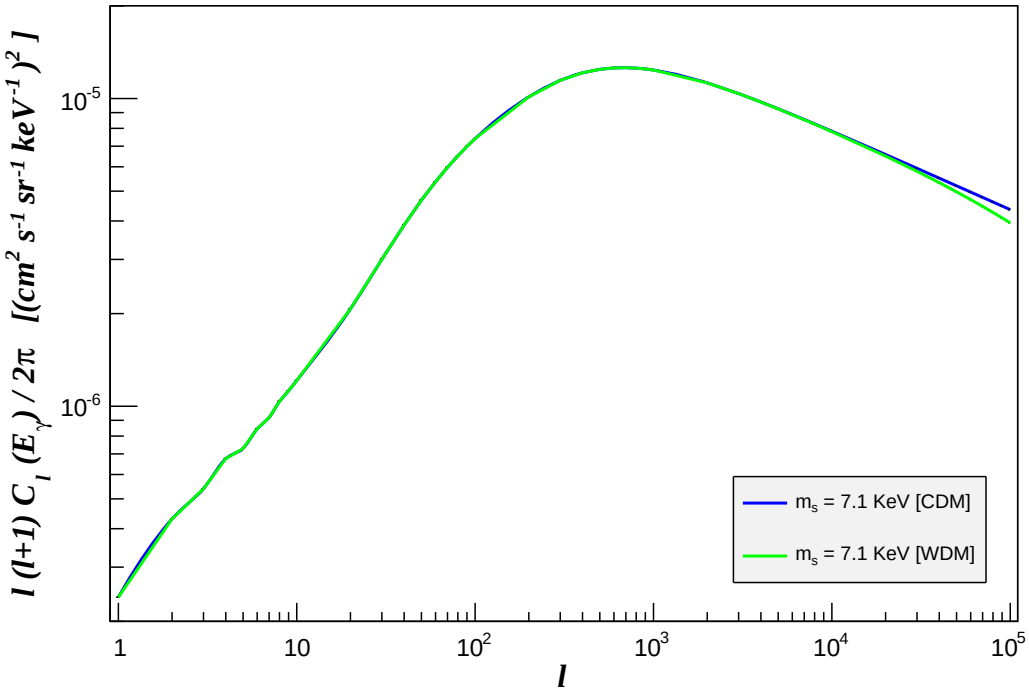

Figure 4.11: Comparison between the APSAC of a decaying CDM (*blue* curve) and a WDM (*green* curve) sterile neutrino with $m_{\rm s} = 7.1$ keV, relative to the sensitivity of eROSITA. The values of the mixing angles are: $\theta^2_{\rm as} = 1 \times 10^{-10}$ for the first and $\theta^2_{\rm as} = 2 \times 10^{-11}$ for the second.

Table 4.2: Comparison of $C_l^{\rm CDM}$ with $C_l^{\rm WDM}$ predicted for Astro-H, in the $m_{\rm s} = 7.1$ keV case.

l	$C_l^{\rm CDM}$	$C_l^{\rm WDM}$	$\Delta C_l = C_l^{\rm CDM} - C_l^{\rm WDM}$	$\Delta C_l / C_l$
1	8.73×10^{-8}	8.73×10^{-8}	3.18×10^{-17}	3.64×10^{-10}
10	8.5×10^{-7}	8.5×10^{-7}	6.13×10^{-15}	7.21×10^{-9}
10^2	5.44×10^{-6}	5.44×10^{-6}	2.72×10^{-12}	5.01×10^{-7}
10^3	1.25×10^{-5}	1.25×10^{-5}	3.07×10^{-10}	2.45×10^{-5}
10^4	8.02×10^{-6}	8.01×10^{-6}	1.17×10^{-8}	0.00146
10^5	4.46×10^{-6}	4.19×10^{-6}	2.8×10^{-7}	0.0626

This feature is consistent with the prediction that the power spectrum in the WDM case is lower than the CDM at small scales, corresponding to high multipoles. This suggests that the same considerations exposed in the previous section also apply to this case and strongly indicates that, in the energy scale considered, there is barely no distinction between WDM and CDM $\nu_{\rm s}$. We conclude that neither Astro-H nor eROSITA will be able to discern between CDM and WDM scenarios, in the case in exam of $\nu_{\rm s}$ DM, as the difference between the corresponding C_l values is very small.
To better highlight the tiny difference between $C_l^{\rm CDM}$ and $C_l^{\rm WDM}$, in Table 4.2 these two values are listed, together with their absolute and fractional differences, for six distinct powers of l. Notice how the two APSAC match to a high accuracy for most l values and their separation increases with the multipole, confirming what stated above.

4.3.4 Error estimation

We shall now briefly discuss the error treatment in our calculations, from which the 1-σ uncertainties have been obtained. The errors bars shown in the figures of the previous two subsections are essentially determined by the Poisson noise of the cosmic signal [80] and are evaluated through the following formula

$$\delta C_l = \sqrt{\frac{2}{(2\,l+1)\,\Delta l\,f_{\rm sky}}}\,\left[C_l + \frac{C_{\rm N}}{W_l^2}\right]\,, \tag{4.3.7}$$

where

- W_l is the window function of a Gaussian point spread function

$$W_l = \exp\left(-\frac{l^2\,\theta^2}{2}\right)\,,$$

- $C_{\rm N}$ is the power spectrum of the photon noise

$$C_{\rm N} = \frac{\Omega_{\rm sky}\,(N_\gamma + N_{\rm B})}{N_\gamma^2}\,,$$

  where $N_{\rm B}$ is the number of background photons and N_γ is the number of signal photons

$$N_\gamma = E_\gamma\,\langle I_\gamma(E_\gamma)\rangle\;\Omega_{\rm sky}\,A_{\rm eff}\,t_{\rm exp}\,,$$

where $\Omega_{\rm sky}$ is the angular size of the region in the sky covered by the satellite during the observation time, $A_{\rm eff}$ and $t_{\rm exp}$ are, respectively, the effective area and the exposure time of the device which performs the measurements.

- Δl is the chosen bin of multipole values and
- $f_{\rm sky} = \frac{\Omega_{\rm sky}}{4\pi}$ is the fraction of the sky observed by the satellite.

The precise values of such quantities for the considered devices (Astro-H and eROSITA) are shown in Table 4.1.
Examining Eq. 4.3.7 we can identify the factors which determine the magnitude of the errors bars in the previously shown plots. Above all, W_l^2 is the quantity mainly causing the exponential growth of the error bars, with increasing l. This suggests that the most reliable multipole range that should be examined is $l = [1, 10^3]$ for both eROSITA and Astro-H, as can also be easily assessed from the previous figures.

Chapter 5

Galactic foreground emission $\Phi(\psi)$

Sterile neutrinos decaying within our galaxy can give a strong contribution to the signal from which the APSAC is evaluated. This effect is not expected to be uniform on the entire MW because of the typical distribution of DM in it, as inferred from N-body simulations [81] and astrophysical observations [82]. In the innermost regions of the MW, the DM concentration is such that its decay signal can be so intense to potentially dominate over the cosmic background, originating from distant galaxies and clusters of galaxies. This possibility requires a precise estimate of the Galactic signal, in order to successively subtract it from the observations and to determine the range of Galactic coordinates where the mean extragalactic component will prevail.
In this chapter we shall perform this estimation, first by constructing the general expression of the foreground emission and then by applying it to the specific case of the MW DMH.

5.1 Construction of $\Phi(\psi)$

To determine the Galactic signal we develop the formalism outlined in Sec. 3.2 starting from the *differential flux* [72], defined as

$$\frac{d\Phi(\psi)}{dE_\gamma} = \frac{1}{4\pi}\,\frac{\Gamma_{\nu_\mathrm{s}}}{m_\mathrm{s}}\,\frac{dN_\gamma}{dE_\gamma}\underbrace{\int_0^{s_\mathrm{max}} ds\;\rho_\mathrm{halo}[r(s,\psi)]}_{S_\mathrm{DM}}\;. \tag{5.1.1}$$

where we can read the explicit form of a quantity previously encountered: the DM column density S_DM.
To obtain an expression for Eq. 3.2.1, we integrate the above formula over a desired

energy range $[E_1, E_2]$, giving

$$\Phi(E_\gamma,\psi) = \int_{E_1}^{E_2} dE_\gamma \, \frac{d\Phi(E_\gamma,\psi)}{dE_\gamma}$$
$$= \underbrace{\frac{5.5\times10^{-22}\, s^{-1}\,\theta_{\rm as}^2}{\rm keV}\left(\frac{m_{\rm s}}{\rm keV}\right)^4 \int_{E_1}^{E_2} dE_\gamma\, \delta\left(E_\gamma - \frac{m_{\rm s}}{2}\right)}_{P(E_\gamma)} \underbrace{\frac{1}{4\pi}\int_0^{s_{\rm max}} ds\, \rho_{\rm halo}[r(s,\psi)]}_{J(\psi)} \,, \tag{5.1.2}$$

which has units of $[\mathrm{s}^{-1}\,\mathrm{cm}^{-2}\,\mathrm{sr}^{-1}]$ and where the particle physics factor, $P(E_\gamma)$, and the astrophysics one, $J(\psi)$, are clearly indicated.
Considering the shape of the decay spectrum (cf. Eq. 2.2.2), the choice of $[E_1, E_2]$ is strictly dictated by the value of $m_{\rm s}$, but is also influenced by the energy resolution ε of the measuring apparatus. Furthermore, considering that $\nu_{\rm s}$ decaying within the Galaxy are negligibly redshifted, for a given $m_{\rm s}$ it is sufficient to integrate in a range within the accuracy of the instrument, i.e. $E_{1,2} = m_{\rm s}/2 \pm \varepsilon$.
Now, in oder to compare Eq. 5.1.2 with Eq. 4.2.1, we must integrate the latter over some energy range $[E_1', E_2']$. The choice of E_1' and E_2' should not match that of $[E_1, E_2]$ because, if it did, it would lead to an underestimation of the extragalactic component. Thus, recalling the shape of Eq. 4.2.1 as a function of the photon energy (cf. Fig. 4.1), for a given $E_\gamma = m_{\rm s}/2$, $[E_1', E_2']$ can be set accordingly: e.g., for $E_\gamma = 3.55$ keV, the interval [0 keV,4 keV] accounts for all redshifted photons contributing to the extragalactic component. This then leads to

$$\langle I_\gamma \rangle = P(m_{\rm s}, \theta_{\rm as}^2)\, \frac{\rho_{\rm cr,0}\,\Omega_{\rm DM,0}}{4\pi\,\rm keV} \int_{E_1'}^{E_2'} dE_\gamma\, \frac{1}{E_\gamma\, H(\frac{m_{\rm s}}{2\,E_\gamma} - 1)} \,, \tag{5.1.3}$$

with $P(m_{\rm s}, \theta_{\rm as}^2)$ given in Eq. 4.2.2 .

Having now Eq. 5.1.2 and 5.1.3 the same units, they can be compared. Before doing so, one last thing needs to be specified: a suitable expression for the DM density profile, $\rho_{\rm halo}(r)$, of the MW DMH. In this work three accredited possibilities have been adopted, namely

- the Navarro, Frenk, White (NFW) profile [83]

$$\rho_{\rm halo}^{\rm NFW}(r) = \frac{\rho_{\rm s}}{\left(\frac{r}{r_{\rm s}}\right)\left(1+\frac{r}{r_{\rm s}}\right)^2} \tag{5.1.4}$$

- the Isothermal (ISO) profile [84]

$$\rho_{\rm halo}^{\rm ISO}(r) = \frac{\rho_{\rm s}}{1+\left(\frac{r}{r_{\rm s}}\right)^2} \tag{5.1.5}$$

- the Einasto (EIN) profile [85]

$$\rho_{\rm halo}^{\rm EIN}(r) = \rho_{\rm s} \exp\left[-\frac{2}{\alpha}\left[\left(\frac{r}{r_{\rm s}}\right)^{\alpha} - 1\right]\right] \tag{5.1.6}$$

where $r_{\rm s}$ is the characteristic scale, equal to 20 kpc for NFW and EIN profiles and to 5 kpc for the ISO profile, and $\rho_{\rm s}$ is the normalisation factor. The latter is obtained by imposing $\rho_{\rm halo}(r = R_{\odot}) = 4 \times 10^5\,{\rm keVcm^{-3}}$, i.e. by normalising the DM distribution to the value inferred in the Solar System [77]. α in Eq. 5.1.6 is an extra parameter typical of the EIN profile, which we set to 0.17 following [85].
With this final ingredient, the Galactic signal, $\Phi(\psi)$, can be compared to the extragalactic mean component, $\langle I_\gamma \rangle$. We will do so in the following section, which will also include the discussion of the results.

5.2 Comparison of $\Phi(\psi)$ with $\langle I_\gamma \rangle$

A quick examination of the NFW and EIN profiles evidences how they both diverge as $r \to 0$. For this reason our predictions have only been obtained for the range of angles 5 deg $\leq \psi \leq$ 180 deg, thus avoiding the foreground emission from the Galactic centre. Furthermore, recalling the parametrisation for the galactocentric coordinate $r(s, \psi)$ given in Eq. 3.2.3 and setting $s = R_{\odot}$ and $\psi = 5$ deg in it, the resulting excluded region centered on the MW DMH has radius of ~ 741 pc.
With these elements set, the predictions have been generated in an analogous pattern as that of Sec. 4.3.2, i.e. the first two plots that will follow refer to Astro-H, while the last two to eROSITA; the first of each couple of figures displays the results for $m_{\rm s} = 5$ keV, while the second for $m_{\rm s} = 7.1$ keV. Each plot shows the extragalactic mean intensity $\langle I_\gamma \rangle$ (*blue* curve) together with $\Phi(\psi)$, evaluated assuming a NFW profile (*black* curve), ISO profile (*red* curve) and a EIN profile (*green* curve).

Comparison of Fig. 5.1 with 5.2, and analogously Fig. 5.3 with 5.4, confirms a result from Sec. 4.3.2, i.e. that, between $m_{\rm s}$ and $\theta_{\rm as}^2$, the latter is the parameter mainly controlling the order of magnitude of the intensity. Indeed, although lighter, the 5 keV $\nu_{\rm s}$ leads to both a higher mean extragalactic intensity and also foreground emission (Fig. 5.1), compared to the 7.1 keV counterpart (Fig. 5.2). Comparing instead Fig. 5.1 with Fig. 5.3, and equivalently Fig. 5.2 with Fig. 5.4, evidences another characteristic already discussed in Sec. 4.3.2: the greater luminosity detected by Astro-H compared to eROSITA. Although the mean extragalactic component, $\langle I_\gamma \rangle$ (*blue* curve), detected by eROSITA and Astro-H differ imperceptibly, the foreground emission observed by Astro-H at each ψ, $\Phi(\psi)$ (*red*, *green* and *blue* curves), is slightly higher than that measured by eROSITA. This difference is, again, attributable to the greater spectral resolution of the Astro-H.

The results of our investigation for the ψ values at which $\langle I_\gamma \rangle > \Phi(\psi)$, for each of the four cases discussed, are reported in Table 5.1. Since there is still uncertainty on which of the three utilised mass profiles is the most adequate to describe the DM distribution within the MW, we can conservatively assume the most stringent directions of observation found among those listed in the table. Despite this cautiousness, however, the message

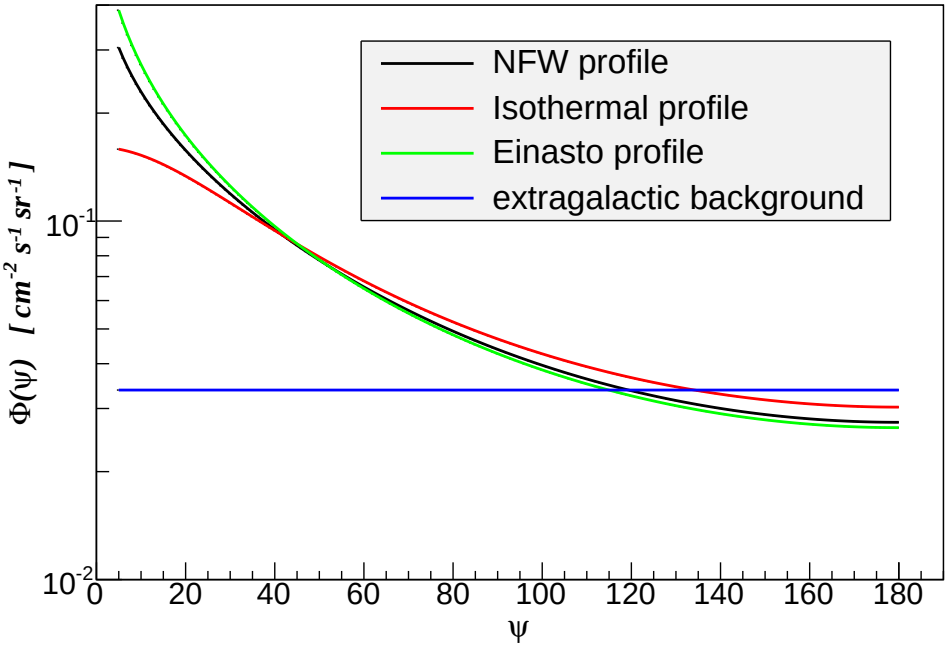

Figure 5.1: Mean extragalactic intensity $\langle I_\gamma \rangle$ (blue curve) compared to Galactic signal, $\Phi(\psi)$, assuming a NFW profile (black curve), ISO profile (red curve) and a EIN profile (green curve); prediction relative to Astro-H. The particle physics parameters adopted are: $m_s = 5$ keV and $\theta^2_{as} = 1 \times 10^{-10}$.

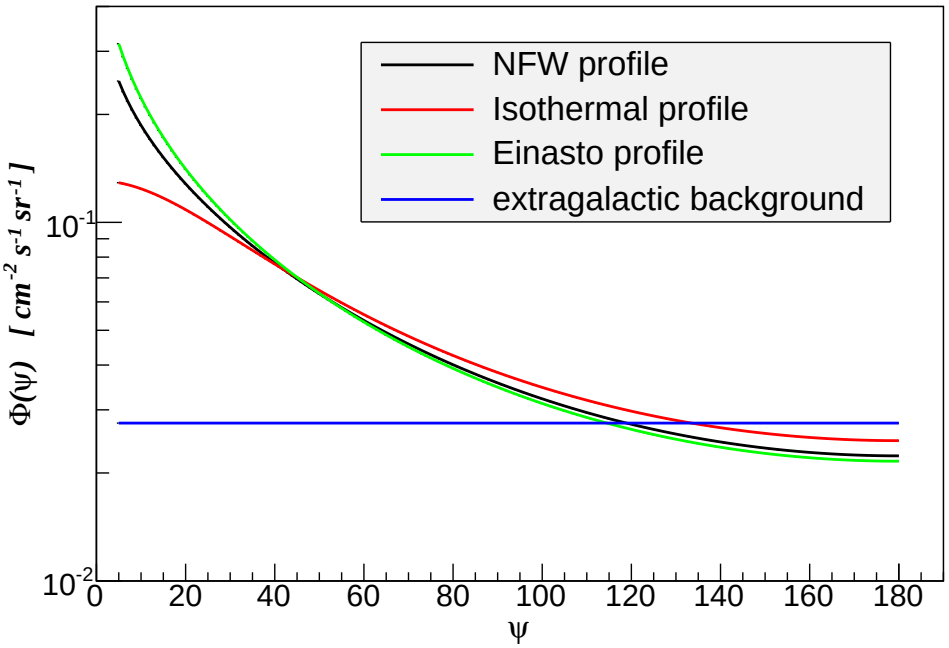

Figure 5.2: Mean extragalactic intensity $\langle I_\gamma \rangle$ (blue curve) compared to Galactic signal, $\Phi(\psi)$, assuming a NFW profile (black curve), ISO profile (red curve) and a EIN profile (green curve); prediction relative to Astro-H. The particle physics parameters adopted are: $m_s = 7.1$ keV and $\theta^2_{as} = 2 \times 10^{-11}$.

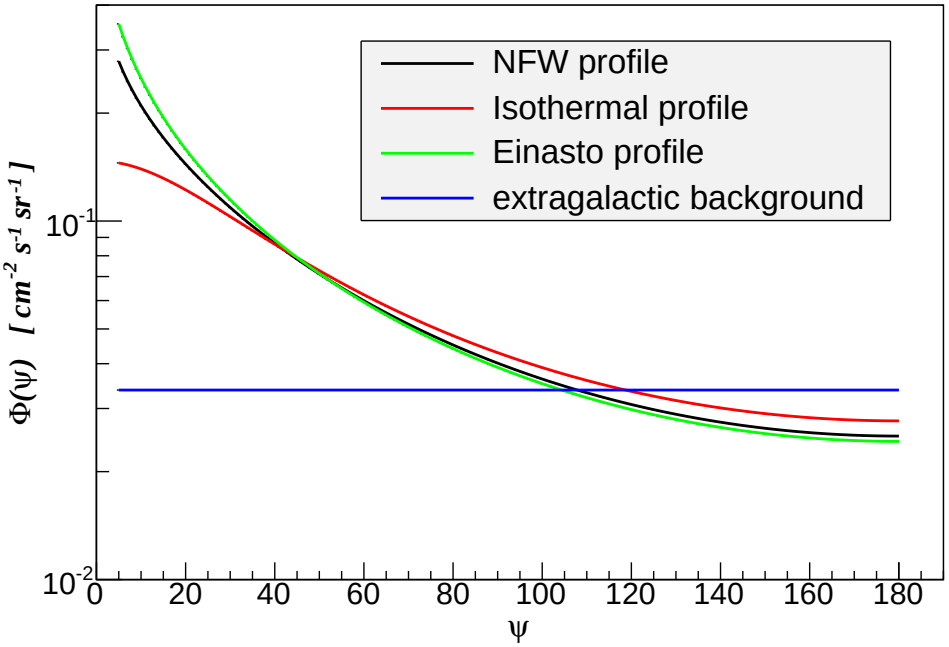

Figure 5.3: Mean extragalactic intensity $\langle I_\gamma \rangle$ (blue curve) compared to Galactic signal, $\Phi(\psi)$, assuming a NFW profile (black curve), ISO profile (red curve) and a EIN profile (green curve); prediction relative to eROSITA. The particle physics parameters adopted are: $m_s = 5$ keV and $\theta^2_{as} = 1 \times 10^{-10}$.

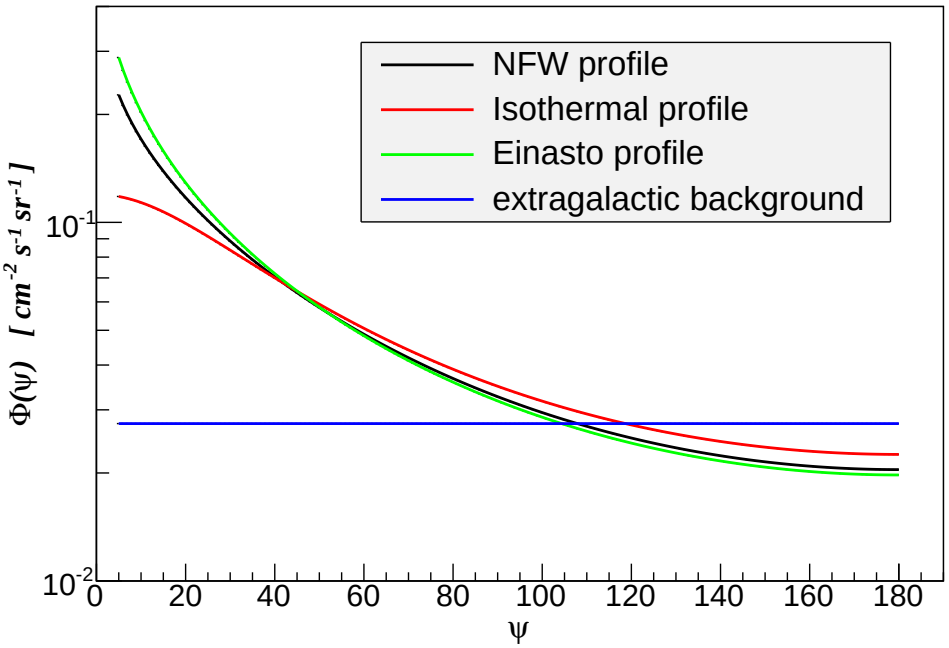

Figure 5.4: Mean extragalactic intensity $\langle I_\gamma \rangle$ (blue curve) compared to Galactic signal, $\Phi(\psi)$, assuming a NFW profile (black curve), ISO profile (red curve) and a EIN profile (green curve); prediction relative to eROSITA. The particle physics parameters adopted are: $m_s = 7.1$ keV and $\theta^2_{as} = 2 \times 10^{-11}$.

Table 5.1: ψ values after which $\Phi(\psi) < \langle I_\gamma \rangle$

	Astro-H ($m_s = 5$ keV)	Astro-H ($m_s = 7.1$ keV)	eROSITA ($m_s = 5$ keV)	eROSITA ($m_s = 7.1$ keV)
NFW	120 deg	119 deg	108 deg	108 deg
ISO	135 deg	134 deg	119 deg	119 deg
EIN	115 deg	115 deg	105 deg	105 deg

contained in those values is unequivocal: In a wide range of angles, the Galactic contribution from decaying ν_s contaminates the X-ray sky of both eROSITA and Astro-H, thus musking the mean extragalactic component of the CXB. Because of its greater spectral resolution, in Astro-H's case this phenomenon is accentuated, as can be deduced from the values in Table 5.1. We can conclude that eROSITA can be preferred to Astro-H in measuring the APSAC of the CXB as it will have access to a slightly wider range of angles, on directions opposite to the Galactic Centre.

We conclude by noticing a very important aspect contained in the plots shown in this chapter. Recalling the characteristics of the two devices considered throughout this work (cf. Table 4.1), we see that the mean extragalactic component of the CXB is in all examined cases sufficiently higher ($\sim$ few $\times 10^{-2}\,\mathrm{counts\,s^{-1}\,cm^{-2}\,sr^{-1}}$) than the background photons detection threshold of both eROSITA and Astro-H. This consideration indicates that, despite the Galactic contribution over a large range of angles, both instruments will have the capacity to observe the ν_s decay cosmic signal. The verification of its detectability would require a precise estimation of the background contamination from astrophysical sources.

Chapter 6

Cross-correlation C_l^{X}

All the predictions obtained so far in this work did not include a detailed calculation of the background contamination. However, several classes of astrophysical sources can give different contributions to the investigated signal. Some examples of such sources are the intracluster medium [86], active galactic nuclei [87] and the interstellar medium of star-forming galaxies [88]. Altogether, these and other sources should yield to an astrophysical X-ray background which can be modeled as a power law with spectral index approximately equal to unity [89]. As previously mentioned (cf. Sec. 2.2.2), the ν_{s} decay line is expected to appear as a spike in spectroscopic measurements of astrophysical objects. This possibility permits to disentangle the surveyed signal from the background by evaluating the cross-correlation of the APSAC, C_l^{X}, with neighbouring energies.
In this chapter we report the motivations for performing this calculation, followed by the results we have obtained.

6.1 C_l^{X} at different energies

As baryonic matter is predicted to be a biased tracer of the underlying DM component [1], astrophysical sources which can emit radiation in the X-ray band are expected to follow the DM distribution to a high degree. Hence their matter power spectrum can be taken - to a first approximation - to correspond to the $P(k, z)$ introduced in Sec. 3.1.1. This means that any process producing photons, different from those expected from the ν_{s} decay (cf. Sec. 2.2.2) but with comparable energies, results in a contamination to the predicted APSAC. The background photons can either originate from the atomic transition of heavy (i.e. mass $\gtrsim$ keV) elements distributed in space, or be part of the continuous emission of some astrophysical process. In the former case, the photon spectrum is discrete and, therefore, undistinguishable from the ν_{s} decay, if the energies are comparable, thus representing a concrete threat to the presented search. In the latter, the continuous emission is superimposed to the ν_{s} decay signal, but the cross-correlation of the APSAC of the two spectra should yield a distinguishable pattern, thus allowing to disentangle one from the other. Recalling the shape of the decay spectrum (cf. Eq. 2.2.2) and its Dirac delta representation (cf. Eq. 4.3.1), we notice that it suffice to cross-correlate the APSAC with energies at a distance of $\pm\ 1\varepsilon$ and $\pm\ 2\varepsilon$ from the expected energy ($m_{\mathrm{s}}/2$), as presented in Sec. 3.3.

6.2 Results

Fig. 6.1 and 6.2 show the cross-correlation of the APSAC predicted for Astro-H and eROSITA, respectively. In both plots, the photon energy $E_\gamma^1 = m_\mathrm{s}/2$, resulting from the decay of a 7.1 keV sterile neutrino, is cross-correlated with the energies $E_\gamma^2 = E_\gamma^1 + \varepsilon$ (*black* curve), $E_\gamma^2 = E_\gamma^1 - \varepsilon$ (*red* curve), $E_\gamma^2 = E_\gamma^1 + 2\varepsilon$ (*green* curve) and with $E_\gamma^2 = E_\gamma^1 - 2\varepsilon$ (*blue* curve).
To interpret such plots we must recall Eq. 3.3.1 and Fig. 4.1, from where we see that the height of the curves is controlled by the magnitude of the mixed term $C_l^{1,2}$. This quantity, in turn, is directly related to the distance between E_γ^1 and E_γ^2 and is determined by the overlap between the curve shown in Fig. 4.1 and a Gaussian centered at E_γ^2 and with width ε. For example, $E_\gamma^2 = E_\gamma^1 - \varepsilon$ will lead to the greatest overlap between the mentioned curves, thus resulting in the greatest $C_l^{1,2}$ term and, consequentially, the lowest C_l^X. These considerations allow us to predict the ordering in height of the curves shown in Fig. 6.1 and 6.2, corresponding to the energies (from lowest to highest): $E_\gamma^2 = E_\gamma^1 - \varepsilon$ (*red* curve), $E_\gamma^2 = E_\gamma^1 + \varepsilon$ (*black* curve), $E_\gamma^2 = E_\gamma^1 - 2\varepsilon$ (*blue* curve) and $E_\gamma^2 = E_\gamma^1 + 2\varepsilon$ (*green* curve). A quick examination of such figures evidences that this is the case in the predictions for Astro-H (cf. Fig. 6.1), despite the overlap between the black and blue curves, but only holds at low l values for eROSITA (cf. Fig. 6.2). This is, once again, the consequence of the greater spectral resolution of Astro-H with respect to eROSITA. Indeed, whereas the separation between the different curves of Fig. 6.1 remains constant across the entire examined multipole range, the broader spectral resolution of eROSITA (cf. Fig. 6.2) leads to an amplification of the differences between the curves, which increases as a function of the multipole.

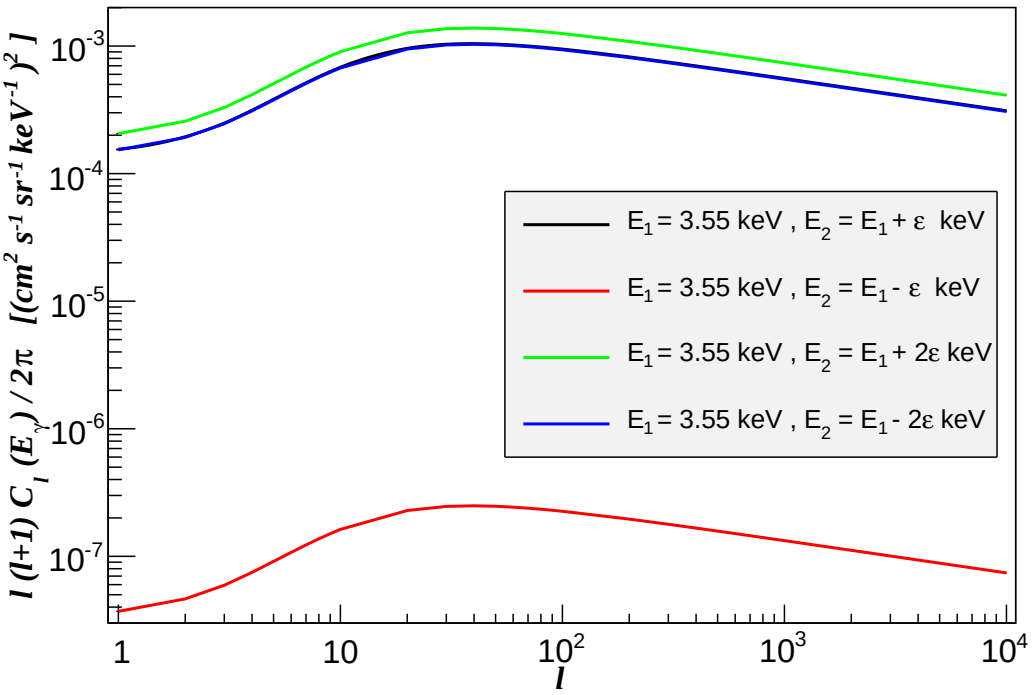

Figure 6.1: Cross-correlation of the APSAC resulting from a $m_s = 7.1$ keV sterile neutrino decay with a photon of $E_\gamma = m_s/2+\varepsilon$ keV (*black* curve), $E_\gamma = m_s/2-\varepsilon$ keV (*red* curve), $E_\gamma = m_s/2+2\varepsilon$ keV (*green* curve) and $E_\gamma = m_s/2-2\varepsilon$ keV (*blue* curve). Prediction associated to Astro-H, for which $\varepsilon = 7$ eV.

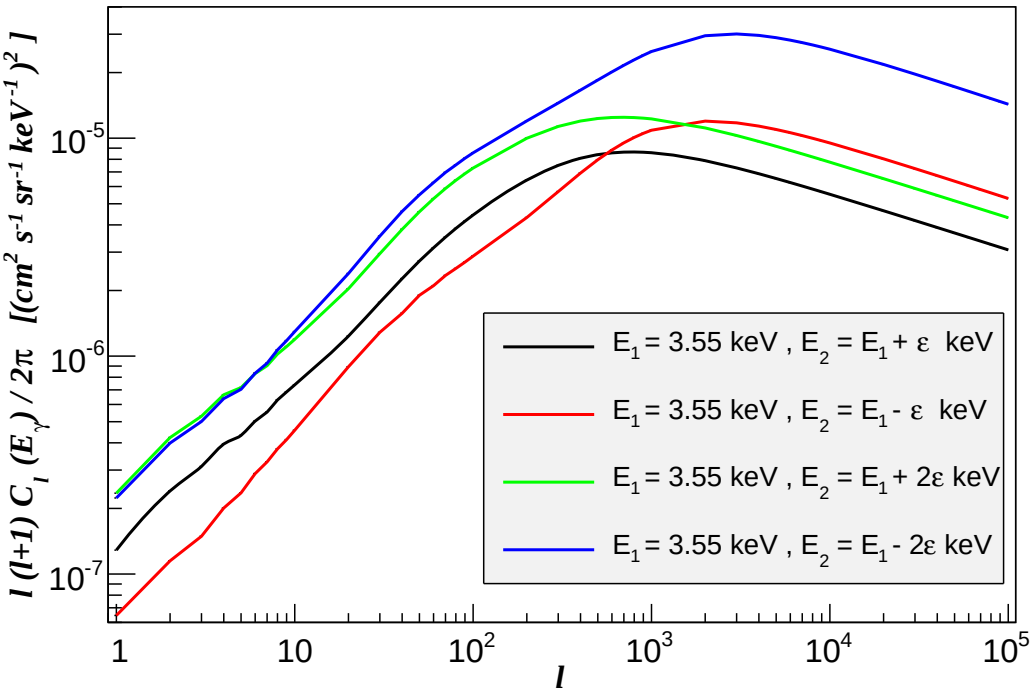

Figure 6.2: Cross-correlation of the APSAC resulting from a $m_s = 7.1$ keV sterile neutrino decay with a photon of $E_\gamma = m_s/2+\varepsilon$ keV (*black* curve), $E_\gamma = m_s/2-\varepsilon$ keV (*red* curve), $E_\gamma = m_s/2+2\varepsilon$ keV (*green* curve) and $E_\gamma = m_s/2-2\varepsilon$ keV (*blue* curve). Prediction associated to eROSITA, for which $\varepsilon = 138$ eV.

Chapter 7

Conclusions

The possibility that DM consists of keV sterile neutrinos has been examined, with special focus on the signatures of their predicted radiative decay. Above all, it has been shown that such decay process should lead to an X-ray background, the CXB, characterised by a particular degree of anisotropy projected onto the sky. Such anisotropy should be directly linked to the spatial distribution of DM in the Universe, which is expressed by the power spectrum $P(k, z)$. The detection of such anisotropy pattern in the angular power spectrum of the CXB emission intensity would represent an uncontroversial evidence for the existence of $\nu_{\rm s}$, in the hypothesis that it constitutes the totality of DM in the Universe. This search can be achieved with two next generation instruments, Astro-H and eROSITA, which will perform in the near future high sensitivity surveys by observing the X-ray sky. Although developed for different scientific purposes, precision spectroscopy of astrophysical sources via deep field observations the former and generation of all-sky maps to study dark energy the latter, the unprecedented high resolution of these detectors opens the possibility to utilise these two devices to indirectly search for DM.

In this work it has been shown that both above mentioned instruments are suitable for performing the search for sterile neutrinos, and we have constructed the predictions for the anisotropy pattern generated by their decay. Such predictions have been generated mainly relative to two claimed values of the sterile neutrino mass, equal to 5 and 7.1 keV, but we have also probed heavier candidates at the energies of 10, 20 and 40 keV. All examined possibilities are consistent with the various constraints available in the literature (cf. Sec. 2.2.3). Along with this calculation, the Galactic signal, due to sterile neutrinos decaying within the Milky Way, has also been estimated as a function of the observation angle ψ, with respect to the Galactic center. This quantity has been compared to the predicted mean isotropic component of the CXB, always originating from the sterile neutrino decay, in order to identify the range of angles where it prevails. It has been found that the Galactic signal should dominate up to angles $\psi \sim 110$ deg, being subdominant only on directions opposite to the Galactic center (i.e. at 110 deg $\lesssim \psi \leq$ 180 deg). Finally, the CXB anisotropic component has been cross-correlated with itself at different energies, these being equal to the spectral resolution of Astro-H and eROSITA or its double. Since the astrophysical background is continuous and can be modeled as a power law, the cross-correlation has allowed to separate the sterile neutrino decay signal from such background, resulting in a specific cross-correlation pattern.

Undesirably, because of the features of the examined DM candidate and the characteristics of the considered instruments, the detection of the expected DM decay anisotropy will hardly allow to discern between WDM and CDM. This is because the predictions obtained in the two distinct scenarios differ slightly and only at the highest multipoles examined, which correspond to the smallest scales observable by the considered instruments.
Because of the greater range of accessible multipoles, the greater richness of features in the predicted signal and, finally, because of the larger range of observation angles where the Galactic contribution is limited, we can conclude that, between the two instruments, eROSITA will be more suitable to perform the presented task.

Bibliography

[1] J. A. Peacock, Cambridge, UK: Univ. Pr. (1999) 682 p

[2] F. Zwicky, Helv. Phys. Acta **6** (1933) 110.

[3] V. Rubin and Y. Sofue Ann. Rev. Astro. Astrophys **39** (2000) 137-174.

[4] M. Roos, arXiv:1001.0316 [astro-ph.CO].

[5] R. Massey, T. Kitching and J. Richard, Rept. Prog. Phys. **73** (2010) 086901 [arXiv:1001.1739 [astro-ph.CO]].

[6] A. Boyarsky, O. Ruchayskiy, D. Iakubovskyi, A. V. Maccio' and D. Malyshev, arXiv:0911.1774 [astro-ph.CO].

[7] K. Jedamzik and M. Pospelov, New J. Phys. **11** (2009) 105028 [arXiv:0906.2087 [hep-ph]].

[8] P. A. R. Ade *et al.* [Planck Collaboration], arXiv:1303.5076 [astro-ph.CO].

[9] T. Clifton, P. G. Ferreira, A. Padilla and C. Skordis, Phys. Rept. **513** (2012) 1 [arXiv:1106.2476 [astro-ph.CO]].

[10] L. Bergstrom, Annalen Phys. **524** (2012) 479 [arXiv:1205.4882 [astro-ph.HE]].

[11] M. Drees and G. Gerbier, arXiv:1204.2373 [hep-ph].

[12] R. Catena and L. Covi, arXiv:1310.4776 [hep-ph].

[13] E. Aprile *et al.* [XENON100 Collaboration], Phys. Rev. Lett. **109** (2012) 181301 [arXiv:1207.5988 [astro-ph.CO]].

[14] B. Dutta, arXiv:1403.6217 [hep-ph].

[15] S. Funk, arXiv:1310.2695 [astro-ph.HE].

[16] A. Aguilar-Arevalo *et al.* [LSND Collaboration], Phys. Rev. D **64** (2001) 112007 [hep-ex/0104049].

[17] A. Kusenko, Nucl. Phys. Proc. Suppl. **221** (2011) 149 [hep-ph/0609158].

[18] K. M. Heeger, hep-ex/0412032.

[19] A. Kusenko, Int. J. Mod. Phys. D **13** (2004) 2065 [astro-ph/0409521].

[20] S. Dodelson and L. M. Widrow, Phys. Rev. Lett. **72** (1994) 17 [hep-ph/9303287].

[21] S. Pokorski, hep-ph/0502132.

[22] L. H. Ryder, Cambridge, Uk: Univ. Pr. (1985) 443p

[23] S. T. Petcov, Lect. Notes Phys. **512** (1998) 281 [hep-ph/9806466].

[24] S. Abe *et al.* [KamLAND Collaboration], Phys. Rev. Lett. **100** (2008) 221803 [arXiv:0801.4589 [hep-ex]].

[25] J. Evans [MINOS Collaboration], Adv. High Energy Phys. **2013** (2013) 182537 [arXiv:1307.0721 [hep-ex]].

[26] C. Giunti and C. W. Kim, Oxford, UK: Univ. Pr. (2007) 710 p

[27] J. M. Conrad, W. C. Louis and M. H. Shaevitz, Ann. Rev. Nucl. Part. Sci. **63** (2013) 45 [arXiv:1306.6494 [hep-ex]].

[28] G. Drexlin, Nucl. Phys. Proc. Suppl. **118**, 146 (2003).

[29] J. Hamann, S. Hannestad, G. G. Raffelt and Y. Y. Y. Wong, JCAP **1109** (2011) 034 [arXiv:1108.4136 [astro-ph.CO]].

[30] S. Hannestad, A. Mirizzi, G. G. Raffelt and Y. Y. Y. Wong, JCAP **1008** (2010) 001 [arXiv:1004.0695 [astro-ph.CO]].

[31] K. N. Abazajian, M. A. Acero, S. K. Agarwalla, A. A. Aguilar-Arevalo, C. H. Albright, S. Antusch, C. A. Arguelles and A. B. Balantekin *et al.*, arXiv:1204.5379 [hep-ph].

[32] A. Gando, Y. Gando, S. Hayashida, H. Ikeda, K. Inoue, H. Ishikawa, M. Koga and R. Matsuda *et al.*, arXiv:1309.6805 [hep-ex].

[33] A. A. Abdo *et al.* [Fermi-LAT Collaboration], JCAP **1004** (2010) 014 [arXiv:1002.4415 [astro-ph.CO]].

[34] G. M. Fuller, C. T. Kishimoto and A. Kusenko, arXiv:1110.6479 [astro-ph.CO].

[35] W. Fischler and J. Meyers, Phys. Rev. D **83** (2011) 063520 [arXiv:1011.3501 [astro-ph.CO]].

[36] C. Tao, EAS Publ. Ser. **53** (2012) 97 [arXiv:1110.0298 [astro-ph.CO]].

[37] X. -D. Shi and G. M. Fuller, Phys. Rev. Lett. **82** (1999) 2832 [astro-ph/9810076].

[38] L. Wolfenstein, Phys. Rev. D **17**, 2369 (1978).

[39] A. Kusenko, Phys. Rept. **481** (2009) 1 [arXiv:0906.2968 [hep-ph]].

[40] M. Shaposhnikov and I. Tkachev, Phys. Lett. B **639** (2006) 414 [hep-ph/0604236].

[41] K. Kadota, Phys. Rev. D **77** (2008) 063509 [arXiv:0711.1570 [hep-ph]].

[42] M. Hoeft, J. P. Mucket and S. Gottlober, Astrophys. J. **602** (2004) 162 [astro-ph/0311083].

[43] P. B. Pal and L. Wolfenstein, Phys. Rev. D **25** (1982) 766.

[44] K. Abazajian, G. M. Fuller and W. H. Tucker, Astrophys. J. **562** (2001) 593 [astro-ph/0106002].

[45] J. Madsen, Phys. Rev. D **44**, 999 (1991).

[46] S. Horiuchi, P. J. Humphrey, J. Onorbe, K. N. Abazajian, M. Kaplinghat and S. Garrison-Kimmel, Phys. Rev. D **89** (2014) 025017 [arXiv:1311.0282 [astro-ph.CO]].

[47] K. Markovi and M. Viel, Publications of the Astronomical Society of Australia / Volume 31 / January 2014, e006 (20 pages) [arXiv:1311.5223 [astro-ph.CO]].

[48] D. HLumb, N. Schartel and F. AJansen, Opt. Eng. **51** (2012) 011009 [arXiv:1202.1651 [astro-ph.IM]].

[49] M. Loewenstein, A. Kusenko and P. L. Biermann, Astrophys. J. **700** (2009) 426 [arXiv:0812.2710 [astro-ph]].

[50] M. C. Weisskopf, H. D. Tananbaum, L. P. van Speybroeck and S. L. O'Dell, astro-ph/0004127.

[51] K. N. Abazajian, M. Markevitch, S. M. Koushiappas and R. C. Hickox, Phys. Rev. D **75** (2007) 063511 [astro-ph/0611144].

[52] A. D. Dolgov and S. H. Hansen, Astropart. Phys. **16** (2002) 339 [hep-ph/0009083].

[53] M. Loewenstein and A. Kusenko, Astrophys. J. **714** (2010) 652 [arXiv:0912.0552 [astro-ph.HE]].

[54] M. Loewenstein and A. Kusenko, Astrophys. J. **751** (2012) 82 [arXiv:1203.5229 [astro-ph.CO]].

[55] E. Bulbul, M. Markevitch, A. Foster, R. K. Smith, M. Loewenstein and S. W. Randall, arXiv:1402.2301 [astro-ph.CO].

[56] A. Bilal, arXiv:0802.0634 [hep-th].

[57] P. H. Frampton, S. L. Glashow and T. Yanagida, Phys. Lett. B **548** (2002) 119 [hep-ph/0208157].

[58] G. C. McLaughlin, J. M. Fetter, A. B. Balantekin and G. M. Fuller, Phys. Rev. C **59** (1999) 2873 [astro-ph/9902106].

[59] A. Kusenko, B. P. Mandal and A. Mukherjee, Phys. Rev. D **77** (2008) 123009 [arXiv:0801.4734 [astro-ph]].

[60] J. Hidaka and G. M. Fuller, Phys. Rev. D **74** (2006) 125015 [astro-ph/0609425].

[61] T. Tsuyuki, arXiv:1403.5053 [hep-ph].

[62] T. Asaka, S. Blanchet and M. Shaposhnikov, Phys. Lett. B **631** (2005) 151 [hep-ph/0503065].

[63] L. Canetti, M. Drewes, T. Frossard and M. Shaposhnikov, Phys. Rev. D **87** (2013) 9, 093006 [arXiv:1208.4607 [hep-ph]].

[64] P. Colin, V. Avila-Reese and O. Valenzuela, astro-ph/0009317.

[65] M. Boylan-Kolchin, J. S. Bullock and M. Kaplinghat, Mon. Not. Roy. Astron. Soc. **415** (2011) L40 [arXiv:1103.0007 [astro-ph.CO]].

[66] M. Drewes, Int. J. Mod. Phys. E **22** (2013) 1330019 [arXiv:1303.6912 [hep-ph]].

[67] A. Cooray and R. K. Sheth, Phys. Rept. **372** (2002) 1 [astro-ph/0206508].

[68] C. Baugh, Encyclopedia for Astronomy and Astrophysics [DOI: 10.1888/0333750888/2136]

[69] P. Monaco, [astro-ph/9710085].

[70] W. Dehnen and J. Read, Eur. Phys. J. Plus **126** (2011) 55 [arXiv:1105.1082 [astro-ph.IM]].

[71] S. i. Ando and E. Komatsu, Phys. Rev. D **87** (2013) 12, 123539 [arXiv:1301.5901 [astro-ph.CO]].

[72] A. Ibarra, D. Tran and C. Weniger, Int. J. Mod. Phys. A **28** (2013) 27, 1330040 [arXiv:1307.6434 [hep-ph]].

[73] J. M. Shull, Astrophys. J. **784** (2014) 142 [arXiv:1401.5799 [astro-ph.CO]].

[74] http://camb.info/

[75] B. A. Bassett and R. Hlozek, Dark Energy, Ed. P. Ruiz-Lapuente (2010, ISBN-13: 9780521518888) [arXiv:0910.5224 [astro-ph.CO]].

[76] A. Merloni, P. Predehl, W. Becker, H. Bohringer, T. Boller, H. Brunner, M. Brusa and K. Dennerl *et al.*, arXiv:1209.3114 [astro-ph.HE].

[77] N. P. Pitjev and E. V. Pitjeva, Astron. Lett. **39** (2013) 141 [Astron. Zh. **39** (2013) 163] [arXiv:1306.5534 [astro-ph.EP]].

[78] T. Takahashi, K. Mitsuda, R. Kelley, F. Aharonian, F. Akimoto, S. Allen, N. Anabuki and L. Angelini *et al.*, Proc. SPIE Int. Soc. Opt. Eng. **7732** (2010) 77320Z [arXiv:1010.4972 [astro-ph.IM]].

[79] M. Viel, K. Markovic, M. Baldi and J. Weller, Mon. Not. Roy. Astron. Soc. **421** (2012) 50 [arXiv:1107.4094 [astro-ph.CO]].

[80] S. 'i. Ando, A. Benoit-Lvy and E. Komatsu, arXiv:1312.4403 [astro-ph.CO].

[81] M. Kuhlen, J. Diemand, P. Madau and M. Zemp, J. Phys. Conf. Ser. **125** (2008) 012008 [arXiv:0810.3614 [astro-ph]].

[82] S. M. Faber and J. S. Gallagher, Ann. Rev. Astron. Astrophys. **17** (1979) 135.

[83] J. F. Navarro, C. S. Frenk and S. D. M. White, Astrophys. J. **490** (1997) 493 [astro-ph/9611107].

[84] M. Ackermann *et al.* [Fermi-LAT Collaboration], Phys. Rev. D **88** (2013) 082002 [arXiv:1305.5597 [astro-ph.HE]].

[85] J. Einasto, Trudy Inst. Astrofiz. Alma-Ata **51** (1965) 87

[86] P. Tozzi, [arXiv:0708.0535 [astro-ph]].

[87] R. Fanali, A. Caccianiga, P. Severgnini, R. Della Ceca, E. Marchese, F. J. Carrera, A. Corral and S. Mateos, arXiv:1305.0564 [astro-ph.HE].

[88] S. Mineo, M. Gilfanov and R. Sunyaev, arXiv:1205.3715 [astro-ph.HE].

[89] A. Moretti, S. Vattakunnel, P. Tozzi, R. Salvaterra, P. Severgnini, D. Fugazza, F. Haardt and R. Gilli, arXiv:1210.6377 [astro-ph.CO].

Acknowledgements

This project has sparked my interest from the beginning, because of its close connection to my previously acquired knowledge in cosmology and for its vicinity to what I have learnt as a GRAPPA master student, but especially because it has largely inspired me and has shown to me what I hope my future as a researcher will be devoted to: phenomenological research on topics at the boundary between cosmology and astroparticle physics. The person I must thank for this is my supervisor, Dr. Shin'ichiro Ando, who has guided me through my first steps in the scientific research. I am profoundly grateful to my two daily supervisors and compatriots, Dr. Irene Tamborra and Dr. Fabio Zandanel, who both patiently helped through the various parts of this work, as good mentors can do, but who also taught me many things that cannot be learnt in textbooks.
I shall not forget to acknowledge the contribution from my classmates and friends Omer, Richard, Laura and Michael. During this experience I have learnt that scientific research can be very stressful and having the right people by your side can make the difference. I would also like to remember other friends and classmates who have supported and helped me in what I feel has been the toughest part of this journey: the first semester at UvA! The support from Giuseppe and Fernando has often been vital for the smooth continuation of my master programme.
A special regard goes to the person who has made this experience a pleasant one, by being by my side and putting up with me in my most difficult moments: my cucciola Mieke.
Finally the greatest thank goes to my family and, in particular, to two persons who have always supported me and believed in me and who will never stop to do so: my father Paolo and my mother Rosanna.